Aalto University
School of Engineering

Samuli Rytömaa

A study on extrinsic cohesive elements for cohesive fracture modelling

Thesis submitted for examination for the degree of Master of Science in Technology.
Espoo 05.09.2016
Thesis supervisor and advisor:
Assistant Prof. Arttu Polojärvi

Aalto-yliopisto
Insinööritieteiden
korkeakoulu

Aalto-yliopisto, PL 11000, 00076 AALTO
www.aalto.fi

Diplomityön tiivistelmä

Tekijä Samuli Rytömaa

Työn nimi Tutkimus ekstrinsisten koheesioelementtien käyttöön koheesiivisessa murtumassa

Koulutusohjelma Konetekniikka

Pääaine Teknillinen Mekaniikka **Koodi** K3006

Työn valvoja ja ohjaaja Apulaisprofessori Arttu Polojärvi

Päivämäärä05.09.2016 **Sivumäärä** 61+5 **Kieli** Englanti

Tiivistelmä

Jään kaltaisten kvasihauraiden materiaalien murtumista voidaan mallintaa koheesiivista särömallia käyttäen. Malli voidaan liittää osaksi elementti-menetelmää käyttäen koheesiivisia elementtejä, jotka voidaan jakaa intrinsisiin ja ekstrinsisisiin malleihin. Ekstrinsinen malli soveltuu paremmin jään murtumisen kaltaisiin tapauksiin, jossa särön kulkureittiä ei tiedetä etukäteen. Yksi tällainen sovelluskohde on jään ja rakenteen välisen vuorovaikutuksen mallintaminen, jossa jäälautta murtuu meriteknistä rakennetta vasten.

Tässä työssä tutkitaan koheesiivisten elementtien käyttöä. Työ sisältää kattavan kirjallisuuskatsauksen koheesiivisen murtuman mallintamisesta ja koheesiivisten elementtien käytöstä. Työn laskennallisessa osiossa kehitetään ekstrinsinen koheesiivinen murtumismalli merijäälle, jota voidaan käyttää jään ja rakenteen välisen vuorovaikutuksen mallintamisessa. Malli perustuu aiemmassa tutkimuksessa kehitettyyn murtumismalliin jota myös käytetään jään ja rakenteen vuorovaikutuksen simuloinnissa.

Tässä työssä tutkitaan myös koheesiivisen murtuman mallintamista kaupallisella Abaqus-elementtimenetelmäohjelmistolla vaihtoehtona itse tehdyille laskenta-malleille. Tällä hetkellä Abaqus sisältää ainoastaan intrinsisiä elementtejä, mutta ekstrinsisiä elementtejä voidaan lisätä käyttäjän itse tekemillä elementeillä. Omien elementtien kehittäminen on kuitenkin haastavaa ja aikaa vievää. Tutkimuksen tuloksena todetaan ettei Abaqus ole käyttökelpoinen vaihtoehto jään ja rakenteen välisen vuorovaikutuksen simuloinnissa.

Työn tuloksena kehitettiin paranneltu versio kaksiulotteisesta koheesiivisesta särömallista, joka toimii alkuperäistä mallia paremmin leikkaussuuntaisissa kuormitustapauksissa. Mallien toimintaa verrattiin MATLAB ohjelmistolla toteutetuilla testeillä. Uusi malli toimii alkuperäistä mallia paremmin leikkaus-kuormitustapauksissa, ja pärjäten yhtä hyvin vetokuormitustapauksissa.

Avainsanat Koheesioelementti, Koheesiivinen murtuma, Merijää, Elementtimenetelmä, FEM

Aalto University
School of Engineering

Aalto University, PL 11000, 00076 AALTO
www.aalto.fi

Abstract of master's thesis

Author Samuli Rytömaa

Title of thesis A study on extrinsic cohesive elements for cohesive fracture modelling

Degree programme Mechanical Engineering

Major Technical Mechanics **Code** K3006

Thesis supervisor and advisor Assistant professor Arttu Polojärvi

Date 05.09.2016 **Number of pages** 61+5 **Language** English

Abstract

Fracture of quasi-brittle materials such as sea ice can be simulated using cohesive crack model. The model can be applied to finite-element method using cohesive elements, which can be divided into intrinsic and extrinsic types. Extrinsic type elements are better suited for simulations where the crack path is not known. One such application is ice-structure interaction simulation, where intact ice sheet breaks against an offshore structure.

In this work the use of cohesive elements is studied, with focus in fracture of sea ice. A state-of-the-art review on cohesive fracture modelling and cohesive elements is conducted. As a computational part extrinsic cohesive fracture model for sea ice is developed for use in ice-structure interaction simulations. The model is based on earlier fracture model used in simulations of ice-structure interaction.

This thesis also includes a study on cohesive fracture modelling using commercial finite-element software Abaqus as an alternative for in-house created codes. At the time Abaqus only includes intrinsic elements, but extrinsic element could be added as user-created element. Creating such elements is challenging and time-consuming, and the study results in Abaqus not being a feasible alternative for ice-structure interaction simulation.

As a result of this work an improved version of the 2-D cohesive crack model is created. The model improves on the original model by in shear dominated cases. Wide variety of tests were conducted using MATLAB to compare the performance between the two models. The new model is found to be better compared to the original model in shear dominated cases, while performing equally well in tensile cases.

Keywords Cohesive element, Cohesive fracture, Sea ice, Finite-element method, FEM

Preface

This master's thesis was done in the ice mechanics research group at Aalto University School of Engineering. The thesis was funded by Tekes - the Finnish Funding Agency for Innovation through project ARAJÄÄ and as well by city of Turku. The financial support is gratefully acknowledged.

I would like to express my deepest gratitude to my supervisor, Assistant Professor Arttu Polojärvi for the guidance given throughout this project. His comments and ideas regarding this thesis have been invaluable. I wish to thank the whole ice mechanics research group for providing a nice working atmosphere and all the discussion regarding ice research and life in general. Additionally I want to thank Professor Pentti Kujala for organizing the opportunity for writing this master's thesis.

Finally I would to express my gratitude to my family, friends and especially my girlfriend Iitu, for all the support and encouragement given throughout my studies. Without you this thesis would not have been possible.

Espoo 05.09.2016

Samuli Rytömaa

Table of contents

1 Introduction

To design safe structures and machines the failure processes must be understood. A structure can fail by either due to yielding or fracture dominant causes. Fracture mechanics have been developed to better understand the fracture process. It concentrates on the analysis of cracks and crack growth. Different mathematical models have been developed to estimate crack growth and life time of structures. Most commonly used method is the linear elastic fracture mechanics pioneered by Griffith. It has been successfully applied to metals and brittle materials such as glass and most ceramics. (Janssen et al., 2004)

One of the main assumptions of the linear elastic fracture mechanics (LEFM) is that the plastic zone or the fracture process zone around the crack tip is small compared to the size of the specimen. In the fracture process zone material behaves non-linearly due to micromechanical phenomena such as yield hardening for metals (Janssen et al., 2004). With materials such as concrete and sea ice the non-linear zone can be of significant size when compared to the specimen size and some ductility is included in the fracture. This removes the applicability of linear elastic fracture mechanics. (Dempsey & Mulmule, 1997)

To overcome the limitation of the applicability of linear elastic fracture mechanics for quasi-brittle materials, alternative methods have been created. One of these is the cohesive crack model, also referred as the fictitious crack model. The model was first introduced by Hillerborg (1976) for the fracture of concrete. The main principle of the cohesive crack model presented in Figure 1 is that after a critical stress has been reached, the stress transmitted through the cohesive interface decreases as a function of the separation of the crack sides. This softening represents the different micromechanical phenomena which cause the nonlinear response of the material. In addition to its better applicability to quasi-brittle materials, one of the main advantages of cohesive cracks over linearly elastic

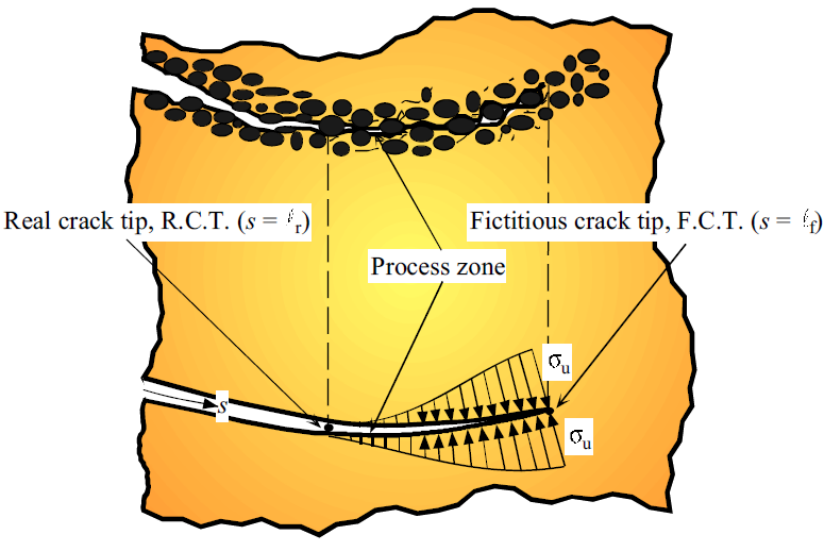

Figure 1. Main principles of cohesive crack model. The crack process zone is modelled as a fictitious crack where part of the stress is transmitted through the interface. σ is the stress transmitted through the cohesive interface. (Carpinteri et al., 2003)

fracture mechanics is its ability to model crack initiation in addition to the crack propagation. The energy used in the fracture process comes directly from the definition of cohesive behavior. The model is also quite easy to implement into finite-element method code. This means that cohesive cracks can be used to simulate the whole fracture process.

The cohesive crack model can be implemented into finite-element method (FEM) using so-called cohesive elements. These are interface elements that are inserted between the continuum elements in the finite-element mesh. The cohesive crack model has been used since its first introduction in wide variety of applications. Most common applications are related to bi-material interfaces such as composite laminates (Alfano & Crisfield, 2001; Camanho et al., 2003; Daudeville et al., 1995) as well as particle reinforced materials and coated materials (Spring, 2015). In these types of analyses the cohesive crack model is used to represent the interface between the two materials. Analysis types where the crack path is not known include impact analysis of brittle materials (Camacho & Ortiz, 1996), dynamic fracture analysis (Zhang et al., 2007), failure of concrete (Hillerborg et al., 1976; Gálvez et al., 2002) and failure of sea ice (Paavilainen et al., 2009; Hilding et al., 2011). In these types of analyses the cohesive elements are used to represent possible crack surfaces.

1.1 Sea-ice fracture

The fracture process of sea-ice plays an important role in the estimation of ice loads on offshore structures in Arctic and Antarctic environments. When an intact ice-sheets comes into contact with an offshore structure, the ice sheet breaks down into smaller blocks as demonstrated in Figure 2. These blocks can form a rubble pile in front of the structure depending on the shape of the structure. After the rubble pile is formed the ice sheet proceeds to fail against the rubble pile. The failure mechanism depends on the shape of structure

Figure 2. A large ice rubble pile that has formed in front of Kemi I lighthouse. (Image by the courtesy of Mauri Määttänen.)

as well as the mechanical properties of ice. Analytical equations have been used to estimate the ice loads on structures. They are obtained through simple analysis based on the estimated failure mechanism. However the estimation of ice loads is hard due to the possibility of interaction between different failure modes that can occur during the ice-structure interaction. Understanding the whole process is necessary for creating better and more accurate analytical models, and better design procedures.

The ice-structure interaction process can be studied using either full scale measurements, model scale tests or computer simulations. Full scale tests give true but limited amount of measurement data, and are also difficult and expensive to perform. Model scale tests are performed under controlled environment in special facilities. The tests can be monitored reliably and the results are easier to reproduce when compared to full-scale tests. Model scale tests are somewhat expensive and time consuming to perform, but they are cheaper than full scale measurements. The scaling of the results to full scale may lead to wrong conclusions. Alternatively, the interaction process can be simulated using computer models. Computer simulations are cheaper and faster alternative to model scale tests and can be done using full-scale parameters. Simulations can provide data which is very difficult to measure in the real world. Computer models must be validated using either model scale or full scale data both qualitatively and quantitatively. (Paavilainen et al., 2011)

When simulating the ice structure interaction process, the ice sheet must be able to break into smaller pieces of ice anywhere in the ice sheet length. The cohesive crack model is a very good candidate for modelling sea ice failure in this type of simulation, due to its ability to model crack initiation and its relatively easy implementation to FEM. Cohesive elements have been used in ice-structure simulation using both commercial programs (Hilding et al., 2011; Kuutti & Kolari, 2012; Lu et al., 2014) as well as in-house developed programs (Paavilainen et al., 2009).

At Aalto University ice mechanics research group ice-structure interaction on sloped structures is simulated using in-house developed 2D combined finite-discrete element method (FEM-DEM) based computer code (Paavilainen et al., 2009). It can model the whole ice rubbling process from intact ice sheet to a complete rubble pile. FEM is used to model the elastic continuum as well as the fracture process. The movement and interaction of ice-blocks is modelled using discrete element method (DEM). An example of the simulation is presented in Figure 3. The code uses beam elements to tie together rectangular discrete elements. This way the blocks model the elastic continuum of an intact ice sheet. Cohesive crack model is applied at the center of each beam element. After the crack has propagated through the beam element, the bond between the two discrete elements is removed and they can then move away from each other. The code has shown agreement with experimental and full-scale data. (Paavilainen et al., 2011)

A more detailed study on the cohesive crack model used in the FEM-DEM code has shown that there are some problems in the behavior of the model in shear dominated cases. These include problems in the amount of energy dissipated, and they are caused by the model formulation. Therefore the model needs to be improved to allow more accurate simulations to be performed.

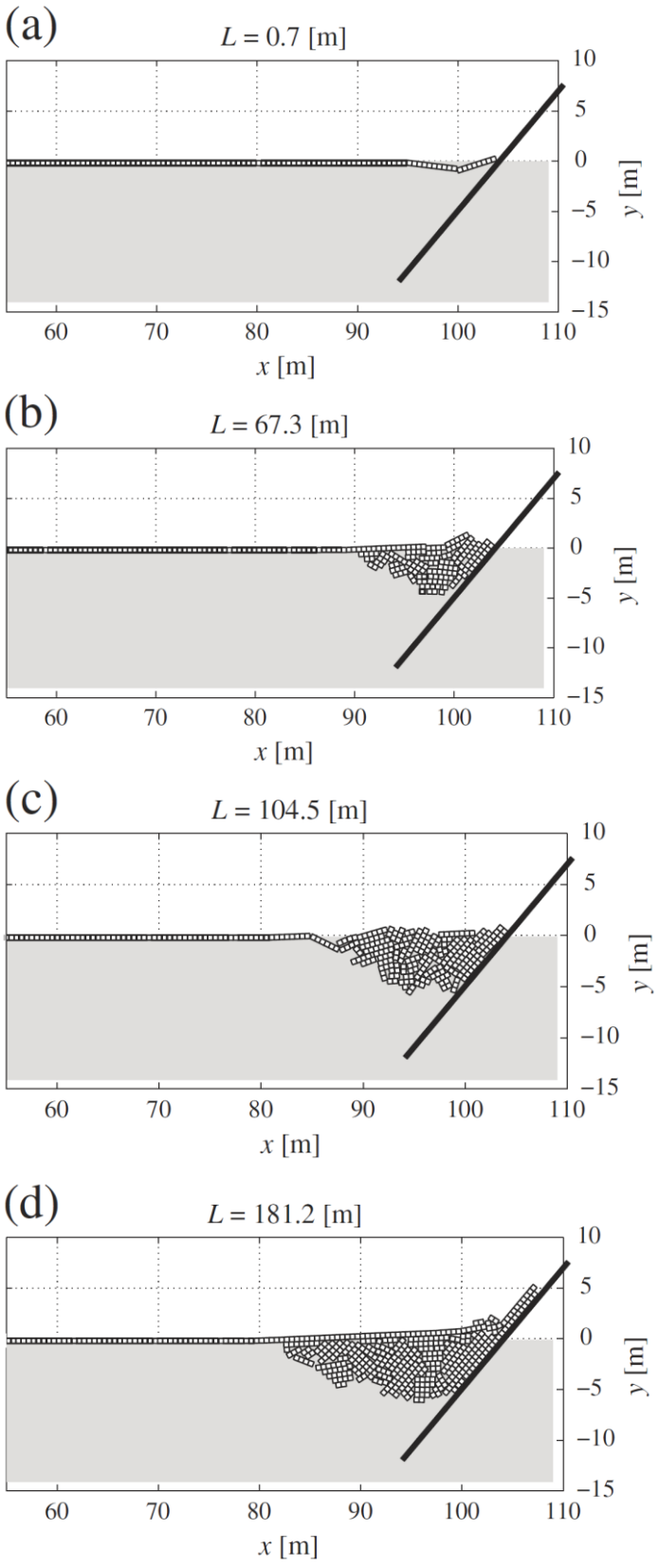

Figure 3. Snapshots of the simulated rubble formation process. *L* is the length of the pushed ice. (Paavilainen et al., 2011)

1.2 Objectives and scope

This thesis is a study on cohesive crack modelling. The study includes a general literature review on the theory of the cohesive crack model and its FEM-applications. The numerical part of the thesis concentrates solely on the sea ice fracture modelling using cohesive elements.

The main objective of this thesis is to develop an improved version of the cohesive crack model used in the Aalto FEM-DEM code. The improved model is implemented into MATLAB, which is also used for the testing of the new model. The main working principles of the new model will be similar to the original model to allow easier implementation to the FEM-DEM code. The main interest is in so-called 'extrinsic' type of cohesive elements, which suits better to simulations where the crack can initiate freely. The improved model is not implemented into the Aalto FEM-DEM code in this thesis.

Additionally, the use of commercial FEM-software Abaqus in cohesive fracture modelling will be evaluated. The aim is to find whether Abaqus could be a viable alternative for the FEM-DEM code. The investigation is performed using a simple test analysis. General modelling aspects are evaluated against the Aalto FEM-DEM code.

1.3 Thesis structure

The thesis is divided into four separate sections. The first section includes the literature survey on the cohesive crack model. The second section evaluates the performance of Abaqus in cohesive fracture modelling. It includes the model creation and the analysis of the results. The third section includes the formulation of the improved cohesive crack model created for the FEM-DEM code and its implementation to MATLAB. In the result section the performance of the new model is compared to the original using different test cases. The thesis is concluded with analysis on the results obtained from the comparison, and conclusions made during the thesis.

2 Cohesive crack model

Cohesive crack model was first presented by Hillerborg et al. (1976) on fracture of concrete. The main advantages of their method is its ability to model both crack formation and the crack growth. Other methods used in crack growth analysis (such as LEFM) cannot model the initiation of the crack. This makes it a powerful tool in FE-simulations. The method applies well for sea ice, which is similarly to concrete a quasi-brittle material. Quasi-brittle materials have mostly brittle behavior, but show small amount ductility during the fracture process.

In this chapter, the main ideas of the cohesive crack model are presented, as well as the key points in its application to FE-analysis. The focus is on general theory behind cohesive cracks, but examples related to fracture of sea ice are given.

2.1 General behavior

The advancing cohesive crack can be divided into three different zones, as demonstrated in Figure 4. The first zone is the undamaged area, where the softening has not yet started. When a critical stress has been reached, the cohesive crack zone is formed. In this zone the material is partly damaged, but some of the stress is still transmitted through the interface. As the crack opens more, the amount of stress transmitted decreases. The third zone is the true crack zone, where the macro crack tip starts. In this zone, the crack opening displacement has reached the critical crack opening. No stress is transmitted through the interface on this zone. (Gálvez et al., 2002)

In one dimensional cohesive crack model, the crack is assumed to open when the stress σ at the crack tip reaches the critical stress σ_{cr}. This is the maximum stress that can be transmitted through the cohesive zone. Prior to the formation of the crack the continuum follows its corresponding material model such as linear elasticity. As the crack opens, the stress does

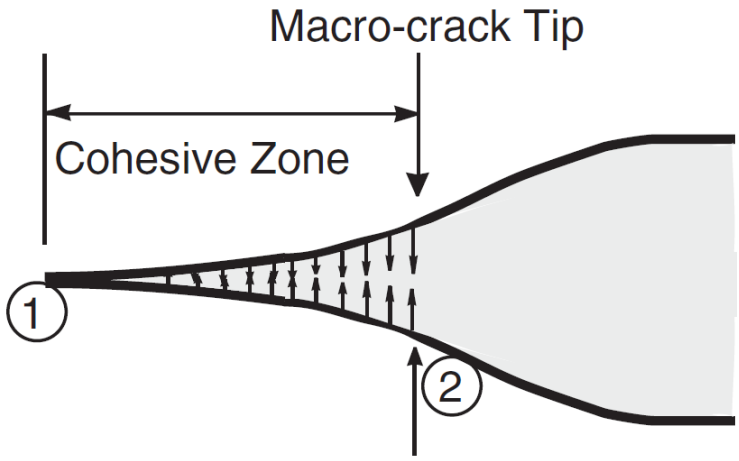

Figure 4. Different zones of cohesive fracture. On the left of 1 is the undamaged area. Cohesive zone is in the middle, and the true crack zone starts at the macro-crack tip. No stress is transmitted through the interface right of 2. (Zhang et al., 2007)

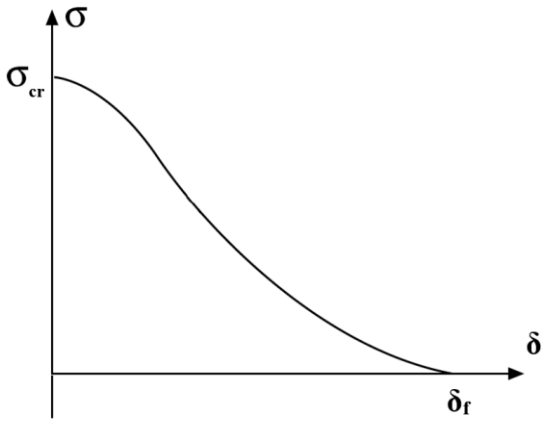

Figure 5. An example of stress separation curve. Here σ presents the cohesive stress, δ the crack opening displacement, σ_{cr} and δ_f are critical stress and crack opening displacement values respectively and G_f is the energy dissipated during the softening.

not fall to zero immediately, but it decreases with the increasing crack opening displacement δ. The relation between stress and crack opening displacement (COD) can be illustrated using a stress-separation (σ-δ) curve presented in Figure 5. At the critical opening δ_f the stress transmitted reaches zero.

The stress acting over the crack absorbs energy as the crack opens more (Hillerborg et al., 1976). The amount of energy absorbed per unit crack area during the opening from 0 to the critical crack opening is

$$G_f = \int_0^{\delta_f} \sigma(\delta) d\delta, \quad (1)$$

where σ is the stress acting over the crack, δ is the opening and G_f is the specific fracture energy per unit area. The energy absorbed is equal to the area between the stress separation curve and the axis' (Hillerborg et al., 1976).

The cohesive crack area where $\delta < \delta_f$ is not a true crack. It is a representation of the micromechanical phenomena happening at the crack tip. Hillerborg et al. (1976) assumed that the cohesive behavior for concrete is due to the micro cracking. The idea of micromechanical phenomena has since been expanded and other sources have since been discussed, as presented in Figure 6. The phenomenon varies between different materials, and the scale can vary from atomistic bonds to much larger fiber bridging. All of the possible explanations for the cohesive behavior give a physical explanation to the cohesive stress (Planas et al., 2004). In some materials the reason is very clear, for example in fiber composites, while in some materials the reason is not so clear. Cohesive behavior can also result from multiple different phenomena. For sea ice possible phenomena are grain boundary sliding and separation as well as micro cracking (Mulmule & Dempsey, 1999).

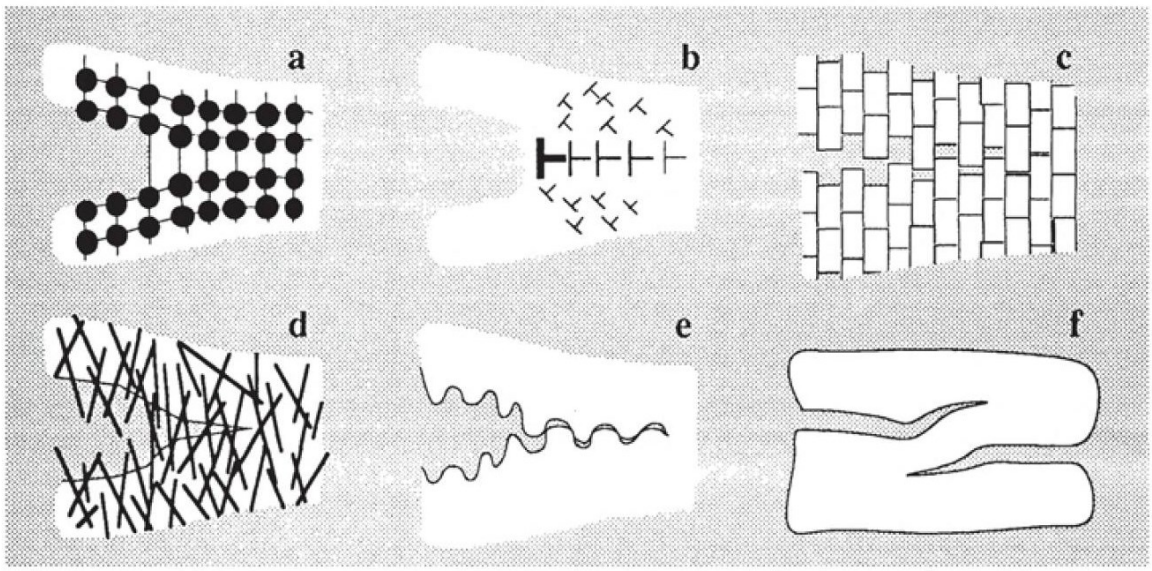

Figure 6. Some of the different physical sources for cohesive forces: a) atomic bonds b) yield strip, c) grain bridging, d) fiber bridging, e) aggregate frictional interlock, f) crack overlap (Planas et al., 2004)

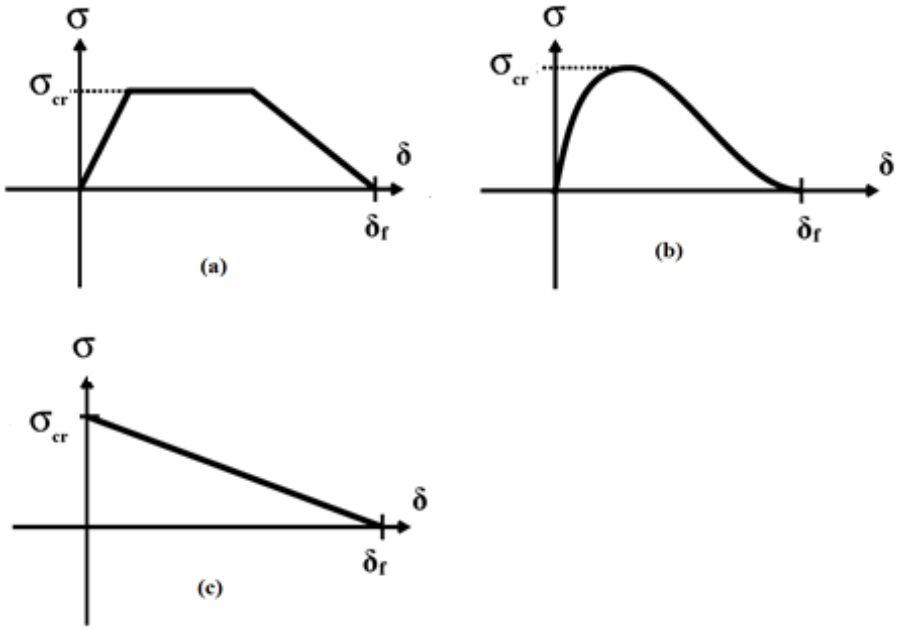

Figure 7. Some examples of different softening functions: (a) tri-linear, (b) continuous and (c) linear (van den Bosch et al., 2006).

One of the key parameters of a cohesive crack is the softening function. The softening function defines the cohesive behavior after the critical stress has been reached. The softening function can be considered as a material property. For each material, the softening function is obtained from experiments. Commonly used softening functions are linear, bilinear and exponential functions, but also other softening functions are used. (Bažant & Planas, 1998) Some examples are shown in Figure 7. Softening functions can be either continuous or defined in parts. In continuous models a single function is used to define the

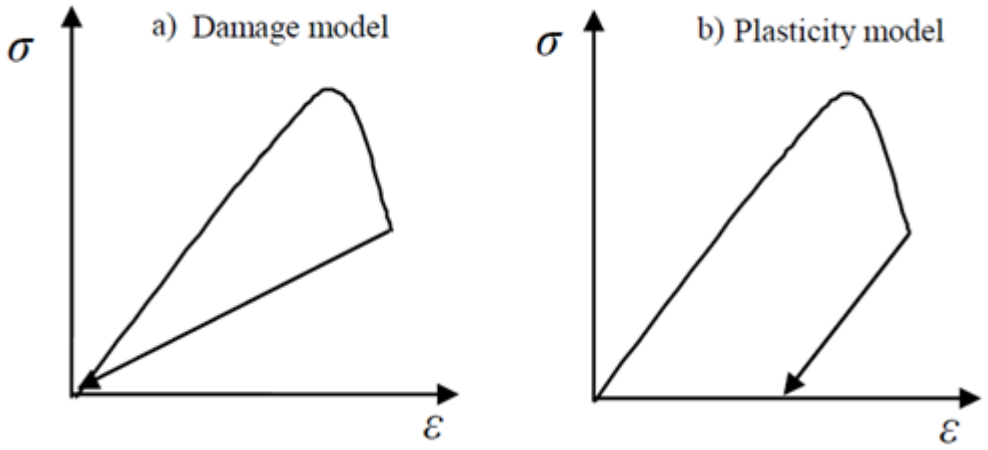

(a) (b)

Figure 8. Difference on unloading behavior between plasticity and cohesive models (Kolari, 2007).

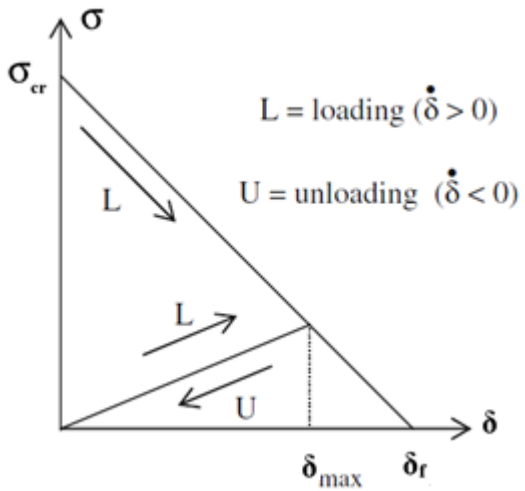

Figure 9. Example of the unload-reload relationship with linear softening. The reload follows the same path as the unloading. (Block et al., 2007)

whole cohesive behavior. This potential based model is discussed later. (Park et al., 2009) Softening functions defined in parts such as the trilinear softening in Figure 7 (a) use simple equations to define the cohesive behavior for selected crack opening range. For sea ice, the softening function is not well defined, but a linear variant has been back-calculated by (Dempsey & Mulmule, 1997).

The softening is irreversible in the way that the reduction of stiffness is permanent. In the case of unloading where δ drops to zero, the stress transmitted also returns to zero as demonstrated in Figure 8 a. This behavior is therefore different when compared to plasticity (Figure 8 b), where some plastic strain remains when load drops to zero. During the reloading process, the stress follows the same path as in unloading as presented in Figure 9. The softening continues after the original softening curve is reached. (Bažant & Planas, 1998)

Linearly elastic materials usually have a linear loading-unloading behavior regardless of the shape of the used softening function. Other shapes for the unload-reload behavior can be introduced.

As demonstrated in Equation (1), the specific fracture energy is defined by the used softening function, critical stress and critical crack opening. In case of a linear softening function, the specific fracture energy is obtained from

$$G_f = \int_0^{\delta_f} \sigma d\delta = \frac{\sigma_{cr}\delta_f}{2} \tag{2}$$

The specific fracture energy and the critical stress can be measured from experiments. In the case of linear softening function they can be used to define the final shape of the softening function and the critical crack opening. Therefore, the critical crack opening can be solved from (2), and it is

$$\delta_f = \frac{2G_f}{\sigma_{cr}} \tag{3}$$

The critical crack opening can be solved similarly for other softening functions. With other softening functions, additional measurement data is required to fully define the shape.

Originally, the cohesive crack model was developed for separation in normal direction only (mode-I) due to normal stress. Cracks can also open in other modes by sliding of the crack surfaces (mode-II and mode-III) and in the combination of these modes, also called mixed-mode. Therefore a mixed-mode behavior should be defined for the model to be able to predict fracture in both modes as well as in combination of the two modes. The mixed-mode behavior can be implemented using either coupled or uncoupled behavior. In uncoupled

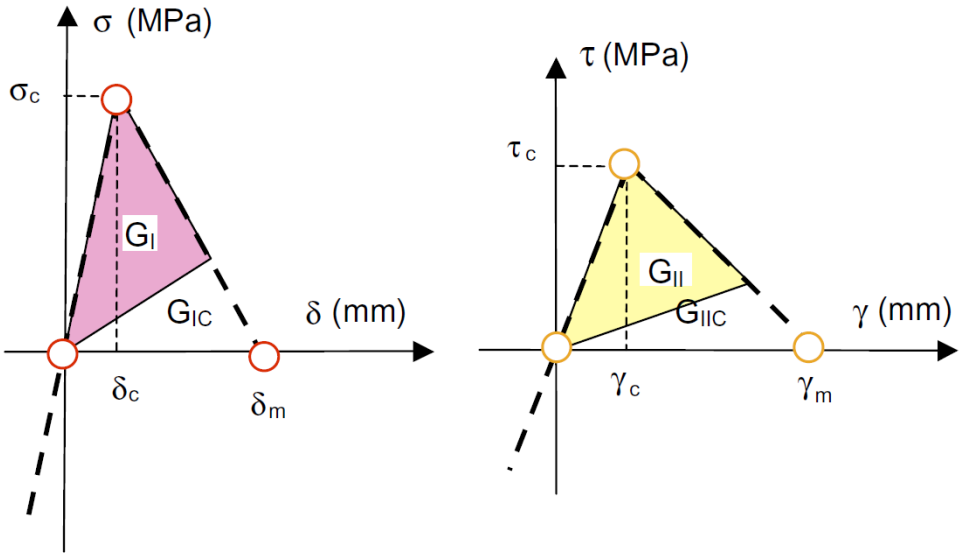

Figure 10. The energy dissipation of uncoupled cohesive model. On the left mode-I and on the right mode-II. The two modes dissipate energy independently based on the respective opening. (Xie & Waas, 2006)

behavior the mode I and mode II are assumed to be independent processes under mixed-mode loading cases. The total energy consumed in the fracture process is the sum of the two components. Both modes have their own stress-displacement graphs as presented in Figure 10. The failure criterion in this case is energy based. This means that the cohesive element is fully damaged when the total energy consumed reaches the specific fracture energy. The model allows different fracture energies to be defined for each mode. (Högberg, 2006; Xie & Waas, 2006) With the addition of mixed-mode behavior, some models have incorporated friction between the cohesive crack faces into the model, which occurs when the crack faces slide in respect to each other. The addition of friction into the cohesive law has been introduced by Camancho & Ortiz (1996).

In coupled case, a special cohesive law is used. A commonly used model is developed by Tvergaard & Hutchinson (1992). This model uses a dimensionless separation parameter to couple the normal and shear modes of the fracture. The coupling forces the fracture energy to be the same in all mode combinations. A commonly used separation parameter is

$$\lambda = \sqrt{\left(\frac{\delta_n}{\delta_{n,cr}}\right)^2 + \left(\frac{\delta_t}{\delta_{t,cr}}\right)^2}, \tag{4}$$

Where δ_n and δ_t are the normal and tangential values, and $\delta_{n,cr}$ and $\delta_{t,cr}$ are the respective opening critical values (van den Bosch et al., 2006). A constant can be used to alter the ratio between normal and shear modes by multiplying the tangential component in Equation (4). This constant is usually based on the ratio between the cohesive strengths of different modes. The constant does not influence the total energy dissipation, if the value of fracture energies are same for all modes. Xu & Needleman (1994) have developed an exponential coupled cohesive law that allows different fracture energies to be defined for each mode. This model is restricted to exponential softening only, and is therefore used less.

Mixed-mode softening models can be divided into potential-based and non-potential-based models. Potential-based models use a potential function to define the constitutive relationship of cohesive fracture. The function represents the fracture energy distribution in conjunction with the separation of fracture surface. This potential has a physical nature, which results in the first derivative providing the traction over the fractured surface. The second derivative gives the constitutive relationship. Potential-based methods are more difficult to create since the potential function must satisfy more boundary conditions such as symmetry, which means that the tangential behavior is identical in both positive and negative directions. The main advantage of potential-based methods is their ability to account for all possible separation and loading paths. With non-potential-based models, non-physical interactions such as positive softening may arise under certain loading conditions Park et al. (2009). Several different potential-based methods have been developed, with one of the most recent by Park et al. (2009). Potential-based models can use either exponential (Xu & Needleman, 1994) or polynomial (Park et al., 2009) potential functions. Polynomial softening functions are more flexible shape-wise and they can have both concave and convex as well as linear shapes. (Park et al., 2009)

For non-potential-based models, a separate failure criterion must be defined to account for mixed-mode cases. There are many different possibilities to define the criterion at which the

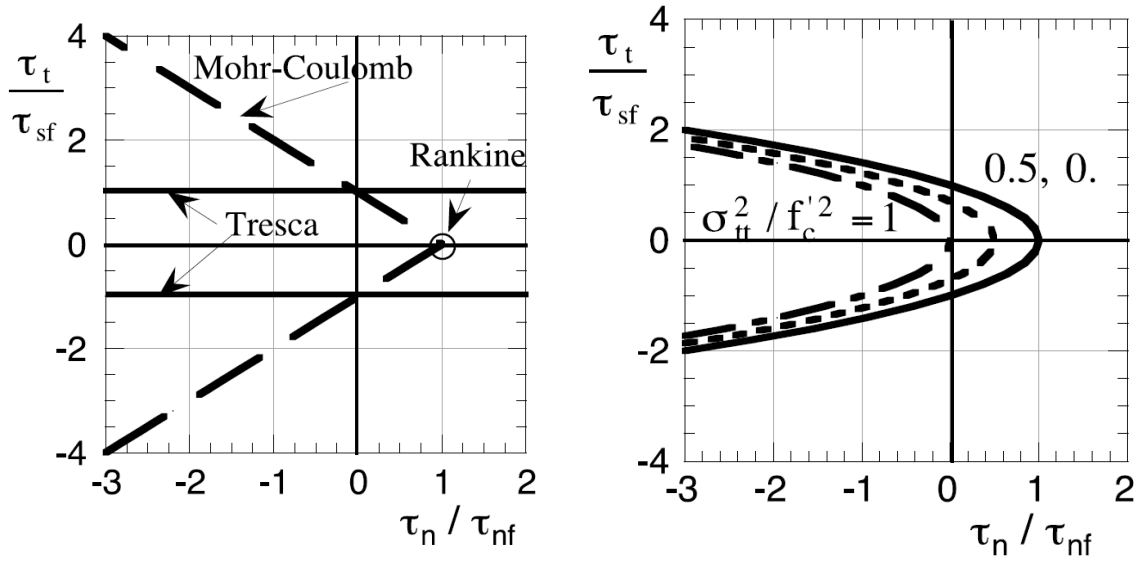

(a) (b)

Figure 11. Rankine, Tresca and Mohr-Coulomb fracture criterions plotted in normal stress-shear stress plane (a). (b) presents the fracture criterion created for sea ice, which combines features from the three classical criterions presented in (a). (Schreyer et al., 2006)

cohesive softening starts. Commonly used failure criterions for quasi-brittle materials are Rankine, Tresca and Mohr-Coulomb criterions which are illustrated in Figure 11 a. Rankine is a maximum tensile stress criterion while Tresca is maximum shear stress criterion. The formulation of both criterions depend only on one traction component. Mohr-Coulomb criterion involves both normal and shear traction components. The formulation results in compressive failure stress being much higher when compared to tensile failure stress as seen in Figure 11 a. Schulson (2001) observed that none of these three criterions could perfectly predict the failure, and depending on the stress state, some criterions work better than the others. Based on these observations Schreyer et al. (2006) created a new continuous failure criterion that is a combination of the Rankine, Tresca and Mohr-Coulomb criterion. Plotting the Schreyer criterion next to the three classical criterions in normal stress-shear stress plane in Figure 11 b, shows how the Schreyer criterion adapts to these three criterions. When the stress state is compressive, Schreyer criterion acts between the Mohr-Coulomb and Tresca criterion, while in tensile cases the criterion falls between the Mohr-Coulomb and Tresca criterion. The Schreyer model has been adopted to cohesive model by Paavilainen et al. (2009), who added the effect of previous opening. Other possibility for failure criterion is to calculate a combined critical stress from the critical stress components. This is a good approach when effective stress and opening are used, since it removes the need to change the effective stress to stress components. The combined critical stress can be calculated from a selected failure criterion or from the fracture toughness. (Camacho & Ortiz, 1996; Zhang et al., 2007)

The numerical implementation of the cohesive crack in fracture mechanics is done using weight function method. The method can be applied for all crack shapes and sizes, but the weight function must be obtained separately for each crack geometry. In the weight function method the stress-intensity factor is first obtained by integrating the product of weight function and the cohesive stress over the crack length. The crack opening displacement can then be obtained using the stress-intensity factor and weight function. This method has been used to back calculate the fracture energy of sea ice. (Dempsey & Mulmule, 1997) The

weight-function method has been expanded to account for creep deformation, which accounts for time-dependent deformation in sea ice. (Mulmule & Dempsey, 1997) Since the solution for each crack geometry must be obtained independently, the applications of the weight function method are limited. A more often used numerical method is based on finite-element analysis.

2.2 Cohesive elements in FEM

In finite-element analysis, cohesive behavior is created using interface elements, which are inserted between the element boundaries of the continuum elements, referred from now on as bulk elements. This method is also called the cohesive zone method (CZM).

Cohesive elements can be implemented into FEM in two different ways. Most cohesive models use continuum type cohesive elements, in which a cohesive element connects two bulk element edges (2D) or surfaces (3D) to each other. The cohesive law is applied at each integration point for the bulk element shared with the cohesive element. The other way is to use discrete cohesive elements, which are spring-like elements that tie adjacent node pairs together. The discrete implementation is more time efficient in calculation due to lesser number of degrees of freedom (Xie & Waas, 2006) .

The cohesive elements can be divided into two categories, intrinsic and extrinsic. Their difference lies in the undamaged behavior as presented in Figure 12. In the intrinsic model the material behavior is linearly elastic, which means that cohesive element behaves linearly elastic up to fracture. The softening starts after the critical stress level is reached. In the extrinsic model however, there is no crack opening before the critical stress is achieved. Intrinsic elements are widely used due to ease of their implementation into a FE-solver (Park & Paulino, 2012). The failure criterion for intrinsic elements can either be stress based, or

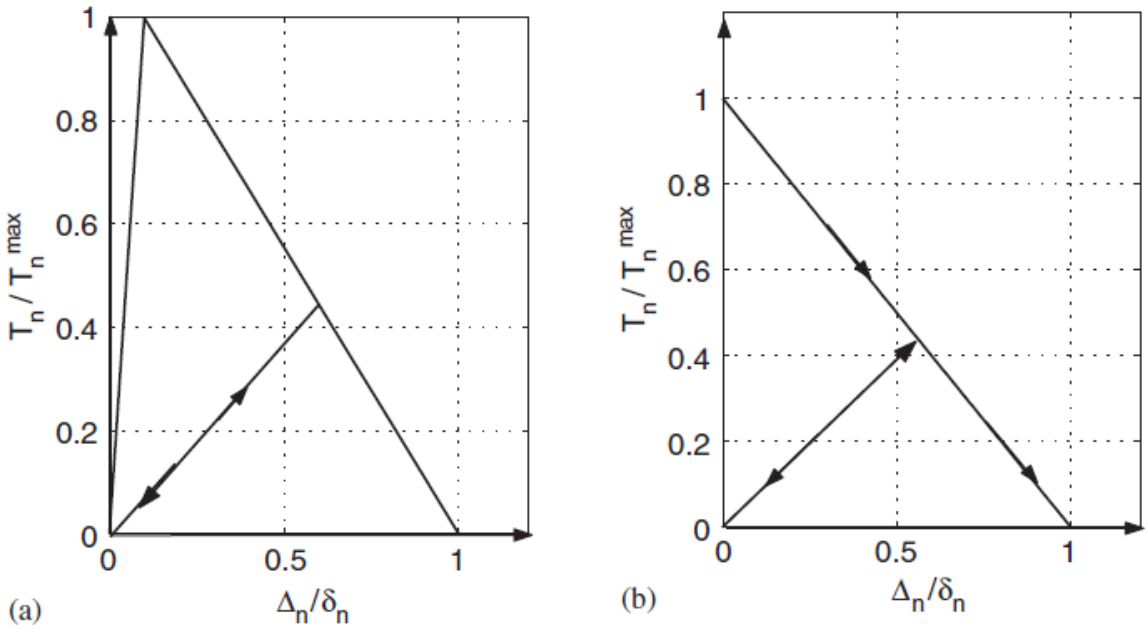

Figure 12. Normalized stress-separation curves for intrinsic (a) and extrinsic (b) cohesive elements. Note the separation before stress starts to decline due to softening in the case of intrinsic element (Zhang et al., 2007).

displacement based. This means that the softening starts when a certain crack opening is reached. Intrinsic elements need to be inserted into the mesh at the start of the analysis, while the extrinsic elements are adaptively inserted to the mesh when the stress between two bulk elements is equal to the critical stress (Sam et al., 2005). The adaptive insertion procedure may lead to additional problems as the so-called time-discontinuity which needs to be addressed. In brief time-discontinuity occurs, when the loads at the element interface before and after element insertion are not equal (Sam et al., 2005).

When using intrinsic cohesive elements, the problem of artificial compliance may rise. This means that the effective stiffness of the mesh is reduced non-physically due to the addition of cohesive elements. The effect comes from the finite initial stiffness of the cohesive element demonstrated in Figure 12 a. The effect is less significant when only one layer of cohesive elements are used, in cases such as delamination simulation. In cases where the cohesive elements are inserted throughout the mesh between bulk elements, the magnitude of artificial compliance increases with decreasing element size. (Sam et al., 2005) A simple one-dimensional analysis shows that the total stiffness of the mesh is (Falk et al., 2001)

$$E_{tot} = E \cdot (1 - \frac{1}{1 + \frac{hE_{coh}}{E}}), \tag{5}$$

where E is the Young's modulus of the bulk material, E_{coh} is the initial stiffness of the cohesive elements and h is the smallest distance between two cohesive elements. As h approaches zero, the material effectively loses all of its stiffness. The reduction is expected to be more severe in both 2D and 3D cases when compared to 1D case.

The artificial compliance can be avoided by increasing the initial stiffness of the intrinsic cohesive elements (Klein et al., 2001). The simplest way to calculate the required stiffness is $E_{coh}=E/t$, where t is the cohesive element thickness. This is applicable when the cohesive layer thickness is small when compared to the bulk material thickness (Daudeville et al., 1995). Since the material effectively loses all of its stiffness when elements are inserted throughout the continuum, the cohesive element thickness is not good parameter to define cohesive stiffness. Additionally the formula is problematic with zero thickness elements. The element spacing h is a good alternative. As can be seen from Equation (5) the cohesive stiffness must be much higher than E/h (Espinosa & Zavattieri, 2003). Turon et al. (2007) proposed that to avoid artificial compliance the cohesive stiffness should be

$$E_{coh} = \frac{\gamma E}{h} \tag{6}$$

Where γ is a parameter much larger than one. For values greater than $\gamma = 50$, the loss of stiffness is less than 2 %.

Cohesive elements with very high stiffness can lead to singularities in the FE-solver, which in turn can prevent the solver from finding the solution for the problem. The FE-solvers can be divided into implicit and explicit types, from which the explicit solver is more prone to the stability issues. In explicit analysis, the time steps used are very small to ensure that the solution is accurate and to avoid numerical stability issues. Because of the small time step, long simulations can take very long times to complete. Implicit analysis applies additional iterations on the solution (such as newton-Raphson iteration) to enforce equilibrium on the

solution. This ensures that the results converge. This is more time consuming per time step, but allows the use of larger time steps. (Bathe, 1996) Due to the equilibrium enforcement implicit solver may be unable to converge into a solution in highly nonlinear problems. Since Aalto FEM-DEM code is used to solve very highly nonlinear problems, it uses explicit solver. Therefore this study concentrates only on explicit methods.

When explicit solver is used, it is important to look at the stable time increment. The stable time increment is a time where the effect of stress waves is removed from the solution. Since explicit solver uses previous state as a starting point for its integration, the time step must be small enough that the elastic wave cannot progress through the smallest element. The critical time step is therefore related to the smallest element length as well as other material parameters that affect the largest wave speed in the material. (Reddy, 2014) This ensures that the solution can converge. The stable time increment can be estimated from

$$\Delta t = t\sqrt{\frac{\rho}{E}}, \tag{7}$$

where E is the stiffness of the element, ρ is the density of the element and t is the thickness of the element. The obtained value is only approximate, and in many cases not safe, which is why the chosen time increment should be lower. (Reddy, 2014; Abaqus, 2014) Thus the value of E_{coh} should be large enough to reduce the effect of artificial compliance, but small enough to avoid any numerical problems. With very high stiffness, the behavior of the intrinsic element approaches the behavior of extrinsic element which does not create artificial compliance due to the initially rigid behavior. (Turon et al., 2007)

Energy dissipated by cohesive elements does not depend on cohesive element size, meaning that the correct amount of energy is dissipated with larger element sizes (Hillerborg et al., 1976). However, since the crack can only propagate on the element borders, the crack path depends highly on the mesh structure. Mesh sensitivity studies have shown that in models with structured meshes, the crack tends to propagate along dominant directions of element alignment. With rectangular elements, the crack follows a zig-zag like pattern, which can cause interlocking in shear (Bažant & Planas, 1998). Additionally, a crack in 45° angle to the element sides will always travel longer distance than the actual crack leading to higher energy dissipation in cohesive fracture. Triangular elements should be used as they allow the crack to propagate more freely. (Xu & Needleman, 1994). Unstructured meshes should be used to reduce mesh dependency in global scale. Additionally, the mesh size needs to be small enough to reduce the effects caused by local mesh orientation. (Guo et al., 2016) Other

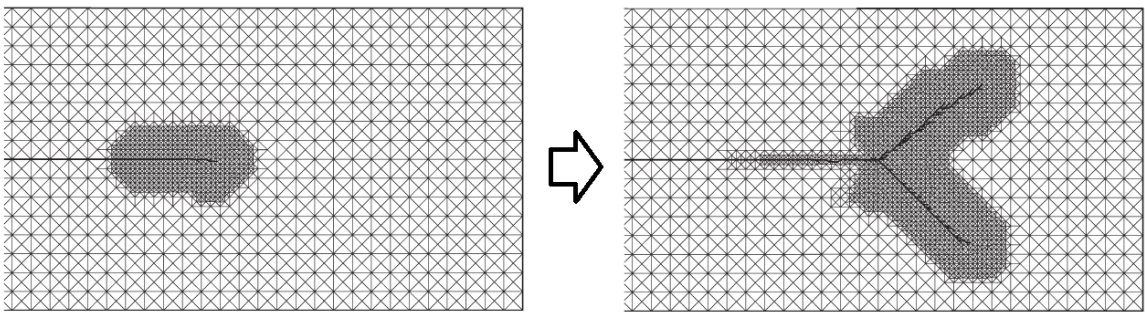

Figure 13. Adaptive mesh refinement and coarsening. (Park et al., 2012)

ways to counter mesh dependency are local mesh update procedures demonstrated in Figure 13, in which the mesh size is reduced near the crack tip during the analysis. This method allows the use of larger overall mesh without reducing the calculation time extensively. The mesh update technique can include both mesh refinement and coarsening. (Park et al., 2012)

3 Modelling cohesive fracture in Abaqus

In this chapter the capabilities of Abaqus 6.14 in cohesive fracture modelling are investigated. Commercial finite-element software packages provide many advantages over in-house created codes. The main advantage is the ease of use. Most of the required features are already included and the remaining can be added to the program as user-created subroutines. More refined user interface makes the modelling and post-processing easier. Commercial programs include already validated solvers, which can be tiresome work for self-created codes. Finally commercial programs are more efficient with advanced algorithms and multi-core operation. All of these features could be included in self-created FE-codes, but a large amount of work is required. Therefore the possibility to use Abaqus, a widely used FE-program, should be studied. (Abaqus, 2014)

In addition to numerous studies involving cohesive fracture of various materials (see, for example (Nguyen, 2014a; Xie & Waas, 2006; Zhou & Molinari, 2004)), Abaqus has been previously used in ice-structure interaction simulations. Lu et al. (2014) used standard features to simulate ice sheet interaction with conical structure, while Kuutti et al. (2013) simulated interaction with inclined structure using user-created fracture routine for ice fracture. Both used cohesive fracture to model the cracking. Heinonen (2004) created a material model for ice rubble that uses cohesive softening for failure. This model does not model discrete cracks, but rather a cohesive softening of the continuum. The model has been used to study AZIPOD thruster interaction with ridges by Kinnunen et al. (2012). Ice rubble interaction with a subsea structure has been studied by Serré (2011) using FEM.

3.1 Cohesive elements in Abaqus

Currently Abaqus includes only intrinsic cohesive elements, but extrinsic cohesive elements have been implemented using user-element subroutine (UEL) (Spring, 2015). In addition to implementing the actual extrinsic element, Abaqus requires a routine for inserting the cohesive elements into the mesh when the critical stress is reached (Papoulia et al., 2003). The lack of extrinsic elements is a clear drawback due to them being better in cases where the crack path is not known.

Abaqus has two modelling possibilities to include intrinsic elements in the analysis. First possibility is to add them by using cohesive elements (Coh3D8), which are inserted into the mesh between the bulk elements. These elements are removed after they are fully damaged. Thickness as well as density need to be defined for the cohesive elements. The layer therefore has mass, but due to small thickness, the total mass of the elements is small compared to the mass of the bulk elements. The other option is to use cohesive interface which can be included in the contact algorithm. This defines cohesive behavior constraint between selected surfaces without additional elements. The general contact algorithm is therefore active during cohesive behavior. The cohesive softening is applied to the integration points in the surfaces selected and uses their stress and displacement data for the fracture and failure criterions. Cohesive elements suppress the contact algorithm while they are active. Cohesive interface does not have thickness or mass. Both implementation techniques require manual work to add the cohesive behavior to the element. This is acceptable in cases where the crack path is known, but when cohesive behavior needs to be manually defined between every bulk element, the work load becomes tiresome. Several subprograms have been developed

to insert cohesive elements throughout the mesh (Carlsson, 2013; Nguyen, 2014b). No such subprograms exist for cohesive interface, which makes cohesive elements more feasible for ice fracture modelling.

Abaqus includes many parameters for cohesive behavior. First of these is the fracture criterion at which the softening starts. The criterion can be based on both mode-specific or combined displacement and traction, for example maximum displacement and maximum quadratic stress. None of the criterions allow pure compressive deformation or stress to initiate damage. Most of the commonly used softening functions such as linear and exponential are included by default, and the user can also define special softening functions using a list of points from the softening function. The final fracture criterion can be either based on maximum opening and total dissipated energy. Defining either total energy or maximum opening defines the other in the case of linear softening as stated in chapter 2. Additional parameters are required for other softening functions. The values of maximum displacement or energy can be different for each mode. The failure criterions can also include the mode-mix ratio between different fracture modes. If no mode-mix ratio is specified, only mode I will be active. In their work Lu et al. (2014) used only mode I in their ice-structure simulations since only fracture energy of sea ice for mode I has been experimentally measured.

3.2 Set-ups for simulations

The cohesive fracture capabilities of Abaqus are investigated using a simple example case under different loading conditions. The aim is to find possible differences between models created using both cohesive elements and interface. Main parameter to analyze is the total dissipated energy as well as the times of fracture initiation and final fracture. General behavior is also studied.

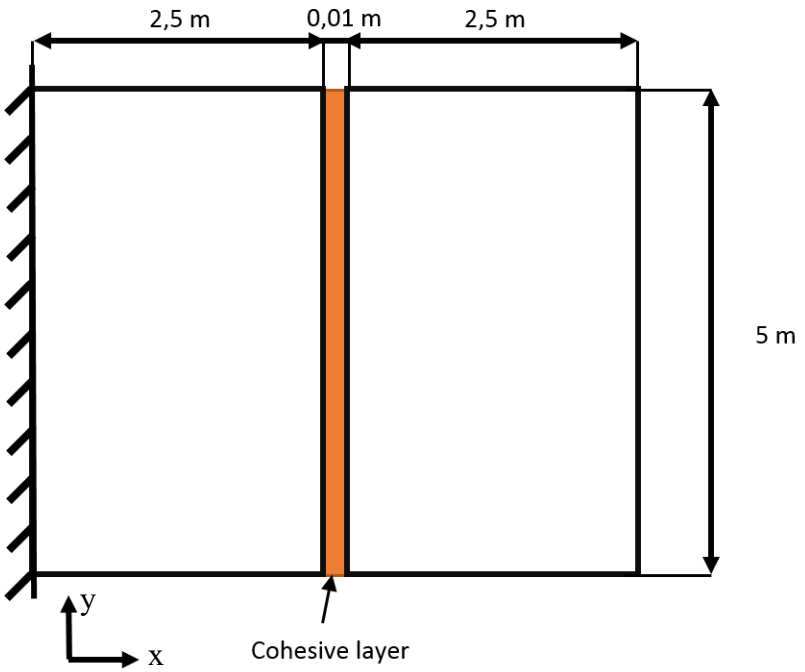

Figure 14. Schematic of the example model. Orange layer represents the cohesive elements.

The example is made of two rectangular blocks that are connected to each other on one side using cohesive elements as Figure 14 shows. The simulation is done in 3D and the thickness of the plate is 0.5 m. The surface area of the crack is therefore 2.5 m^2. Two meshes are compared with each other. Coarser mesh has a mesh size of 0.25 m and finer mesh size is 0.125 m. Both use standard 8 node rectangular solid elements (C3D8), which have 24 displacement degrees of freedom. They don't have any rotational degrees of freedom. The cohesive element size in the cohesive layer is 0.125 m in coarse mesh and 0.0625 in fine mesh. The thickness for both element size is 0.01 m. This means that the cohesive elements are smaller than the bulk elements they are connected to. Abaqus accounts for the mismatched meshes by enforcing the constraint in an average sense over the connected area rather than at discrete points or nodes. (Abaqus, 2014)

Ice is modeled as linear elastic material. Material parameters selected for the simulation are based on Timco & Weeks (2009). The selected values are good estimates for first-year sea ice and they are presented in Table 1. The cohesive interface requires material parameters for critical stresses, fracture energies in different modes and the shape of the softening function. For the cohesive behavior, a linear softening function will be used along with quadratic critical stress criterion and linear energy based mode-mix law. The equation for the fracture criterion is

$$\left(\frac{\langle \sigma_n \rangle}{\sigma_{n,max}}\right)^2 + \left(\frac{\sigma_s}{\sigma_{s,max}}\right)^2 + \left(\frac{\sigma_t}{\sigma_{t,max}}\right)^2 = 1, \quad (8)$$

where σ_n, σ_s and σ_t are the stress components in normal (n) and two tangential directions (s and t) respectively. The "max" subscript denotes the critical stress at in the corresponding direction. The Macaulay brackets $\langle\ \rangle$ define the value of the stress component as zero when $\sigma_n < 0$. The selected criterions are partially similar to the ones used in the Aalto FEM-DEM, which uses combined stress as the fracture criterion and linear softening function. Fracture energy is the same for all modes. Since the surface area of the crack is 2.5 m^2 and G_f= 15 J/m^2, the total energy dissipated during the simulation should be 37.5 J.

Table 1. Material parameters of sea ice used in the simulation.

Parameter	Unit	Value
Density	kg/m^3	920
Young's modulus	GPa	4
Poisson ratio	-	0,3
Friction coefficient	-	0,3
Shear strength	kPa	725
Tensile strength	kPa	540
Fracture energy	J/m^2	15

Table 2. Different load magnitudes and their directions used in the simulation.

Load	Magnitude (kN)	Direction
Shear	1000	Positive y
Tension	2000	Positive x
Compression	200	Negative x
Bending	750	Negative z

The example block is subjected to pure tension, pure shear and pure bending as well as combined shear and tension. The effect of compression on the shear case is also studied by adding compressive load to the shear loaded case. The loads and their magnitudes are listed in Table 2. All of the loads are applied on one side of the block as presented in Figure 15, and the directions of the loads are based on the principal coordinate system shown in Figure 14. A total of 5 different loading conditions are inspected. All of the loads are linearly ramped up from zero to the full force in 80 % of the total simulation time. This is done to avoid dynamic effects caused by sudden load changes. (Borst & Crisfield, 2012) Values for the load magnitudes are enough to cause the fracture, and are not respective to any real loads. Total simulation time is 1 s, in which the fracture occurs.

As presented earlier in chapter 2, artificial compliance is a problem when using intrinsic elements. The effect of artificial compliance is investigated on the tensile loading case. When comparing the example block under tension to one without cohesive elements, larger strains occur in the block with cohesive elements. Without cohesive elements the loaded side has a displacement of 0.70 mm. With a layer of cohesive elements the displacement is 0.85 mm. Clear stress and displacement discontinuities in the bulk material are observed across the cohesive layer as seen in Figure 16. Cohesive layer stiffness was identical to the bulk material stiffness. The effects of artificial compliance can be decreased by increasing the stiffness of the cohesive layer, which decreases the stable time increment in explicit simulation. The stable time increment according to Equation (7) is $5 \cdot 10^{-6}$ s with a Young's modulus of 4 GPa. The critical element length used in the equation for the critical time increment is the cohesive layer thickness. Without cohesive layer the stable time increment is $6 \cdot 10^{-5}$ which is significantly larger. To remove the effects of artificial compliance the stiffness was increased by a factor of 100, based on the recommendation given in Equation (6) by Turon et al. (2007). The increased stiffness reduced the effect of artificial compliance to level that it did not have any significant effect. The increase of element stiffness reduces the stable time increment to $5 \cdot 10^{-7}$ s. The drop is substantial and increases the number of steps required in a 1 second simulation 100 times. Since a single time step takes considerable amount of time, the total simulation time is increased significantly. A slightly smaller time increment of $4.8 \cdot 10^{-7}$ s was selected for the simulation.

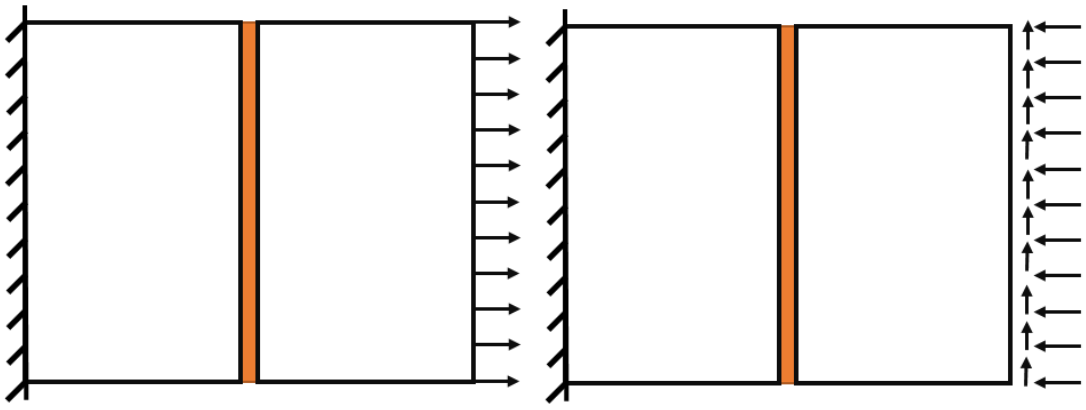

Figure 15. Some examples on the loading cases. On the left is the pure tension and on the right is combined shear and compression.

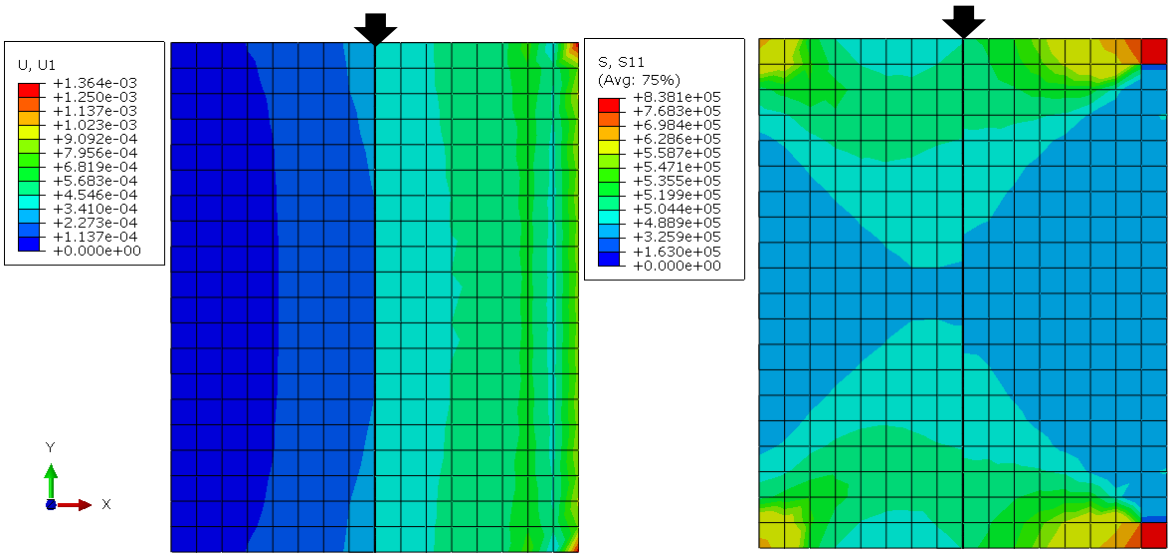

Figure 16. The effects of artificial compliance on the tensile loading case. On the left is the displacement in x-direction, and on the right normal stress in the x-direction. Both show clear discontinuities over the cohesive layer vertically in the middle pointed by the arrows.

3.3 Example case results

An overall review on the results shows that Abaqus can model cohesive fracture well. Finer mesh provides more accurate results, and the accuracy of cohesive elements was better when compared to the cohesive interface. The difference in accuracy increased with larger element size. The results are summarized in Table 3. Figure 17 to Figure 19 show the dissipated energy as a function of simulation time. There is small variation between different models, but mostly the values are close to each other. Cohesive elements are observed to be more accurate than cohesive interface. The fracture happens very fast after the critical stress has been reached as can be seen from the figures. The errors with different modelling methods are also presented in Table 3. The variation of energy levels is still quite small, but in multi-fracture cases this could create a cumulative error.

Table 3. Total dissipated energies and error levels of different models. The correct value for energy dissipated is 37.5 J.

Load combination	Energy with Element coarse [J]		Energy with Element fine [J]		Energy with surface coarse [J]		Energy with surface fine [J]	
Shear	38.4	(2.5 %)	39.0	(4.0 %)	32.5	(-13.3 %)	37.4	(-0.1 %)
Tension	37.6	(0.4 %)	37.6	(0.3 %)	39.5	(5.3 %)	39.6	(5.7 %)
Bending	37.8	(0.7 %)	37.8	(0.8 %)	31.8	(-15.3 %)	37.7	(0.4 %)
Shear + Tension	39.1	(4.1 %)	38.8	(3.4 %)	38.5	(2.6 %)	41.6	(11.0 %)
Shear + Compression	38.3	(2.2 %)	38.8	(3.4 %)	33.1	(-11.8 %)	36.6	(-2.3 %)

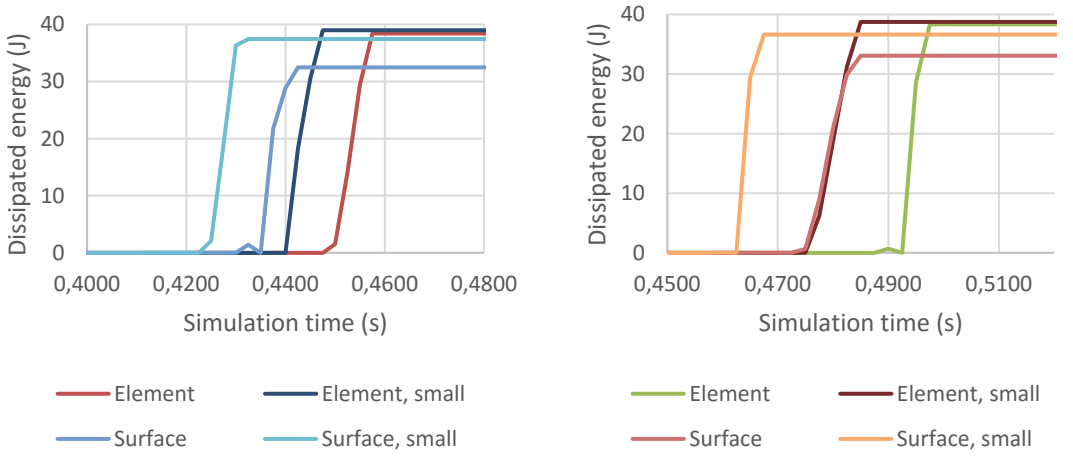

Figure 17. Dissipated energy of different models under shear (Left) and combined shear and compression loading (Right).

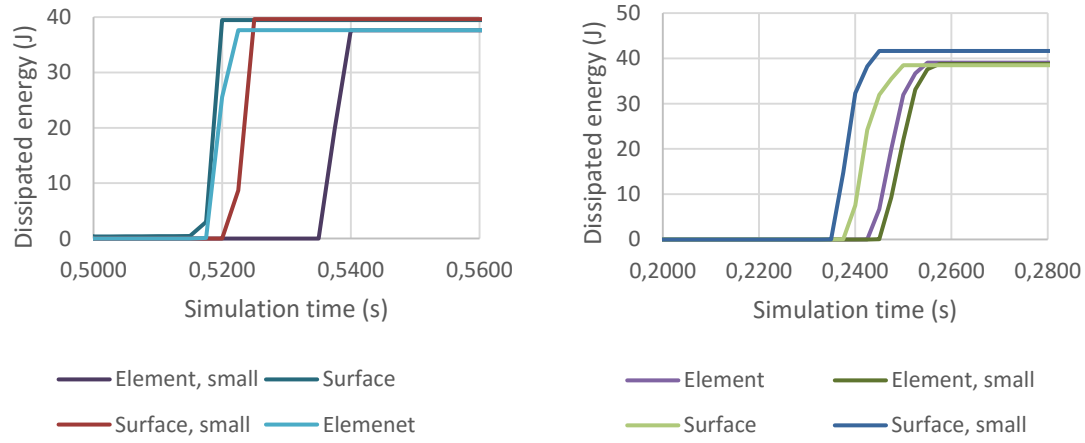

Figure 18. Dissipated energy of different models under tensile (Left) and combined tensile and shear loading (Right).

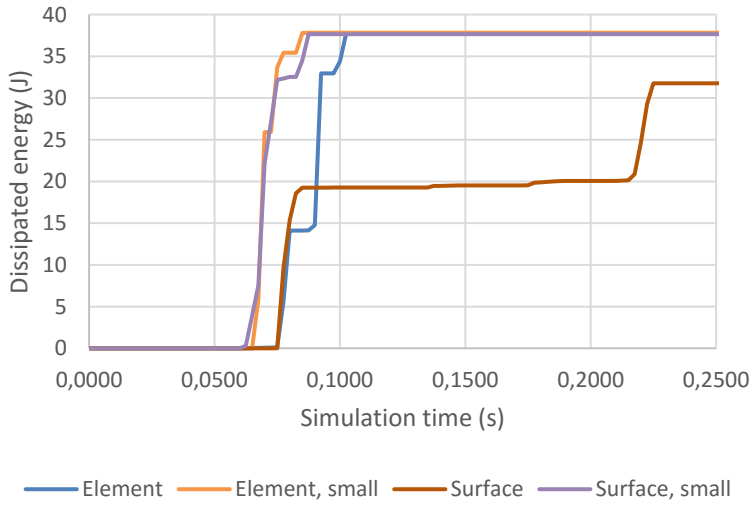

Figure 19. Dissipated energy of different models under bending load.

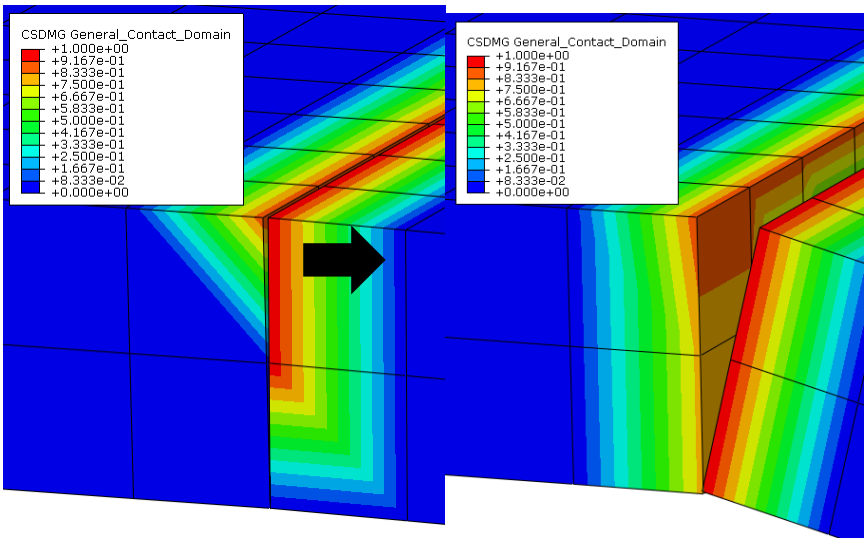

Figure 20. Block rotation in bending case. On the left is the case at fracture stall initiation and on the right is the rotation at the end of fracture stalling.

The differences of fracture loads between different models of the same loading case were quite small as Table 3 shows. The differences between the lowest and largest failure loads were between 3.7-6.0 %. The largest differences were in bending case. In all bending models the failure initiates at roughly the same time, but in coarse surface model the process stalls for 0.09 s, seen as a plateau in Figure 19. This shows that the model does not capture the rotation around the cohesive layer correctly. From the results it can be observed that that the top two node lines break first, after which, the loaded block starts to rotate around the bottom node layer, as seen in Figure 20. This is also indicated by the plateau happening at roughly 2/3 of the maximum energy dissipated. With increased number of elements in the plate thickness direction, the better the model can respond to the bending load. This would prove problematic due to increased calculation time caused by increased number of elements.

The addition of compressive load to the shear load case increases the fracture load, which is expected. With compressive force of 20 % of the shear load the fracture load is increased by 5 %. With higher compressive loads the required fracture load increases even more. As stated earlier, compressive stress doesn't cause any damage to cohesive elements due to the definition of fracture initiation. In the uncompressed case the failure starts at the bottom end of the blocks, where there is also tension as seen in Figure 21. Since the critical tensile stress is smaller than shear stress, this causes the failure to occur earlier. Compression prevents this and forces the failure to be pure shear which requires higher load.

Table 4. Loads at the time of fracture with different models.

Load combination	Load magnitude Element coarse [kN]	Load magnitude Element fine [kN]	Load magnitude Surface coarse [kN]	Load magnitude Surface fine [kN]
Shear	457.5	447.5	442.5	432.5
Tension	1045.0	1080.0	1040.0	1050.0
Bending	76.9	65.6	168.8	65.6
Shear +	S: 255.0	S: 257.5	S: 250.0	S: 245.0
Tension	T: 510.0	T: 515.0	T: 500.0	T: 490.0
Shear +	S: 497.5	S: 485.0	S: 485.0	S: 467.0
Compression	C: 99.5	C: 97.0	C: 97.0	C: 93.5

Table 5. Relative calculation times of different cases.

Load combination	Element Coarse	Element Fine	Surface Coarse	Surface Fine
Shear	1.00	3.28	0.68	2.46
Tension	1.00	3.27	0.67	2.49
Bending	0.98	3.27	0.63	2.27
Shear + Tension	0.98	3.24	0.64	2.35
Shear + Compression	1.00	3.30	0.69	2.47

The required calculation times are presented in Table 5. Fine mesh took 3.3 times more time than the coarse mesh. Cohesive interface based models took only 65-75% of the time taken by cohesive element based models. The cohesive surface algorithm seems be able to calculate the cohesive softening faster. The example was still very simple case, and true ice breaking simulation would have much larger model with multiple failure areas and multiple ice blocks moving and colliding with each other. Finer mesh is required for reasonable accuracy, but it also increases the effect of artificial compliance which reduces accuracy. Countering artificial compliance increases calculation time, as does the finer mesh size. Therefore a balance must be found between the accuracy of the simulation and the calculation time.

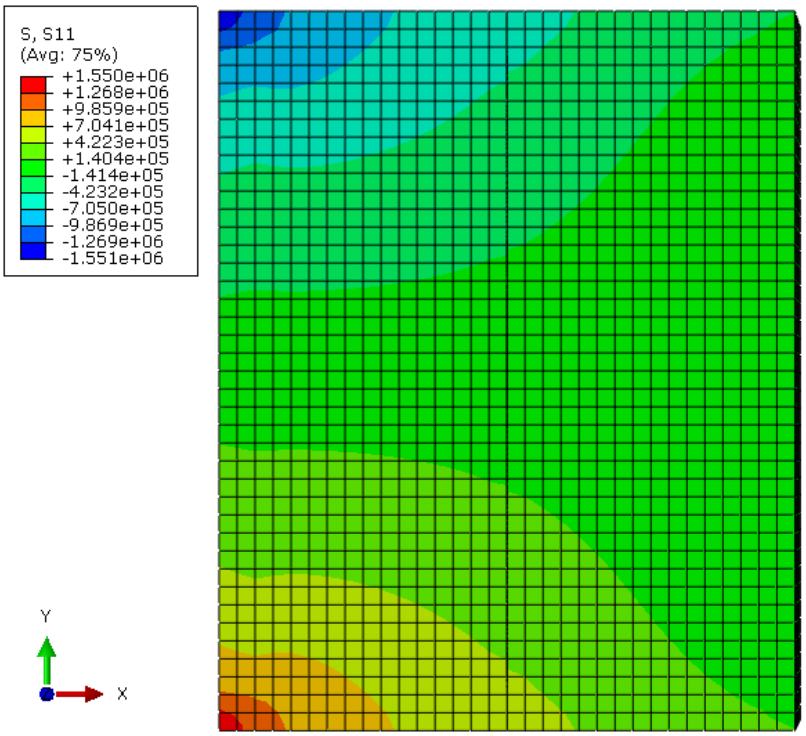

Figure 21. Normal stress distribution under shear loading. The stress on the top side is compressive while bottom is under tensile stress.

3.4 Challenges in ice fracture modelling

Abaqus holds certain advantages and disadvantages in ice fracture modelling when compared to in-house developed FEM-DEM code. The main advantage is that most of the features are already implemented into the software, which allows the user to start modelling immediately. Abaqus already includes many advanced features that could be used in the future, such as more advanced material models that are very easy include in the simulation. In self-created codes the inclusion of such extra calculation routines requires more work and validation. The advantages and disadvantages of Abaqus over in-house created codes are listed in Table 6.

The test results had some variation, and out of the four investigated models none proved to be totally accurate. The cohesive element based model with finer mesh provided the best results by having the best average accuracy in energy dissipation. Cohesive elements are better choice for ice fracture since they can be inserted throughout the mesh and therefore used to model a fracture case where the crack path is not known. The variation in the results shows that the accuracy of the models depends highly on whether cohesive elements or interfaces are used. Further research would be required to analyze the reasons for the inaccuracies. Due to the fact that only intrinsic elements are available this is not feasible.

Currently Abaqus can use only intrinsic cohesive elements, which require short time steps due to high stiffness needed to decrease the effect of artificial compliance. Extrinsic elements are a better choice, but they need to be implemented using user-created subroutines. These in turn require a lot of work in creation and validation, which removes one of the advantages of using commercial programs. Special scripts are also required to insert the extrinsic elements into the mesh when the fracture criterion is satisfied to avoid these problems, but they in turn require additional work and time. Extrinsic elements have been implemented into Abaqus and shown to have good response on fracture cases similar to sea ice fracture. These include multi-fracture and crack branching simulations. (Nguyen, 2014a)

As listed in Table 6, Abaqus holds many advantages over the FEM-DEM code and other self-created calculation routines. The advantages concentrate on the ease of use and already included features. Simulation including the multi-fracture of an ice sheet is still quite small area of research, and some of the features required in the field such as extrinsic cohesive elements are therefore not included in Abaqus. Due to small audience the developers are not interested in adding the missing features to their commercial program. Due to the lack of the required features in ice fracture simulation, the disadvantages outweigh the gains. Therefore alternative possibilities are studied.

Table 6. Advantages and disadvantages of Abaqus over self-created codes in ice fracture modelling.

Advantages	Disadvantages
Validated solver	Only intrinsic cohesive elements
3D FE-simulation	Variation in results
Wide range of modelling options	Work required with user-created subroutines
Ease of use	
Readily available extra features	
Additional features through subroutines	

4 Extrinsic cohesive crack model

Cohesive fracture model used in the Aalto 2D FEM-DEM code is incorporated at the middle of each beam element connecting discrete elements as presented in Figure 22 and is applied in every integration point in the thickness direction of the beam as presented in Figure 23. This means that the crack can progress between each discrete element. Since the same procedure is applied in each integration point, this thesis considers only a case with single integration point. The model includes thousands of discrete elements, which means that there are thousands of possible crack locations. To avoid artificial compliance introduced by thousands of cohesive elements, the cohesive behavior is extrinsic. From the aspect of energy dissipation in fracture, it is enough to study the stress state and energy dissipation in one integration point going through cohesive softening process. In this chapter original model references the FEM-DEM model created by Paavilainen et al. (2009).

The cohesive crack model uses effective stress to model the stress state at the crack. Due to how the effective stress is formed from the stress components in the original model, the mode-II behavior is not captured correctly in shear dominant cases. This results in wrong energy dissipation levels. This can be observed in simple forced displacement tests where the element is loaded in one direction until it fails. This process is then repeated in different directions. The results from such a test are presented in Figure 24, which shows that the model uses wrong amount of energy in tangential direction. Further inspection reveals that final fracture occurs at much larger displacements in shear dominated cases than anticipated. This hints that the used effective stress method does not provide good response in shear dominated cases and the model can be improved.

The aim for this chapter is to create an improved version of the cohesive fracture model used in the FEM-DEM code. The original fracture model will be altered to better account for shear dominated fracture cases. The model is created and tested using MATLAB. To allow better implementation to the FEM-DEM code, the main behavior is kept similar to the

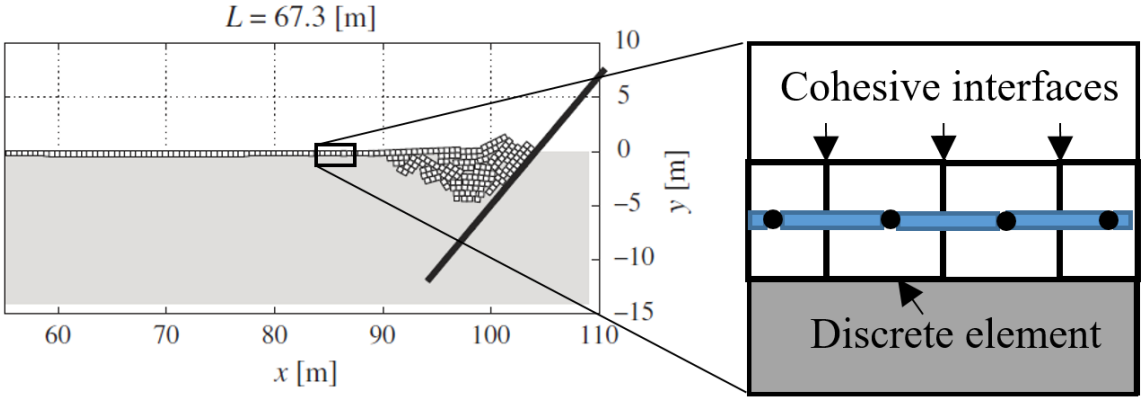

Figure 22. Sketch of the Aalto 2D FEM-DEM code. The blue lines are the beam elements, which connect the discrete elements at their center points (black dots). Cohesive fracture model is applied in the middle of the beam elements, at the boundary of two discrete elements.

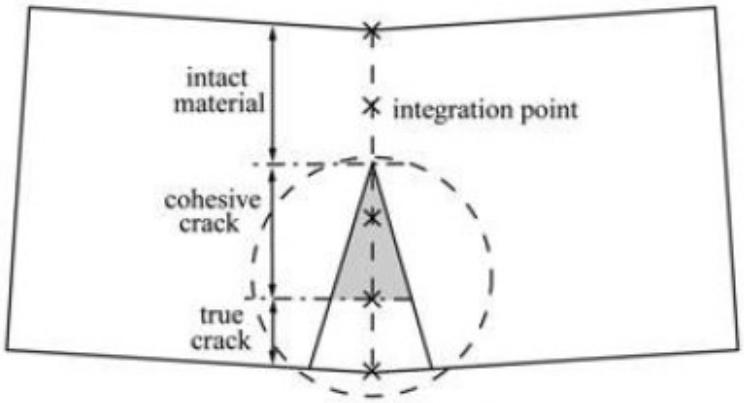

Figure 23. The location of integration points where cohesive crack model is applied in the FEM-DEM code. Integration points in the grey area are experiencing cohesive softening. (Paavilainen et al., 2009)

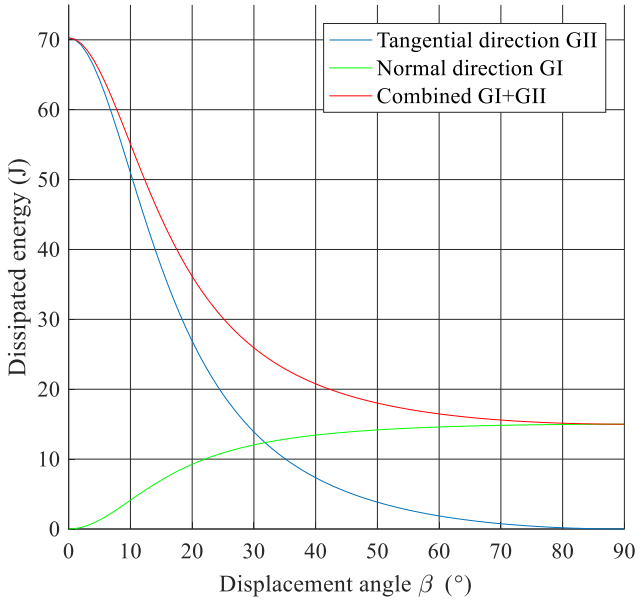

Figure 24. Dissipated energy in the original model. The energy is the fracture energy presented in chapter 2. If the model worked correctly, the red line should be horizontal at 15 J. The curve is the sum of energies dissipated in mode I (GI) and mode II (GII). Displacement angle varies from pure tangential (0°) to pure normal direction displacement (90°).

original model. This way only the equations used in the code need to be altered instead of the structure of the code when the algorithm is implemented into the original simulation program. On the general level both the original and new models work as follows. First, a trial stress based on the total strain is calculated to check whether the fracture criterion is met. If yes, a new crack opening displacement (COD) is calculated based on the trial stress. The new COD is used to return the stress state back to admissible state using the softening function. The whole procedure is covered in more detail during this chapter.

This chapter presents derivation and working principles of the improved extrinsic cohesive crack model in detail. First subchapter presents the fracture criterion and the definition of effective stress and strain. The following subchapter focuses on the cohesive softening behavior. Third subchapter covers energy dissipation, and the final subchapter covers the implementation of the model to MATLAB along with the used test routine.

4.1 Fracture criterion and effective stress measures

The failure of the cohesive element initiates and may progress when the stress state of the material reaches a chosen failure criterion. For this model a stress-based criterion is chosen. The criterion identical to the one used in the original model and it is adopted from the work of Schreyer et al. (2006). The criterion has a following form

$$\frac{\sigma}{\sigma_{cr}} + \frac{\tau^2}{{\tau_{cr}}^2} - 1 < 0, \tag{9}$$

where σ and τ are respectively normal and shear stress components, σ_{cr} and τ_{cr} are respectively critical normal and shear stress values. The directions are based on the fracture plane in the middle of the beam. Normal stress acts normal to the fracture plane, while shear plane is tangential to the fracture plane. The shape of the criterion is presented in Figure 25. The curve is also called a yield surface.

In this work the two dimensional stress state is turned into one dimensional effective stress σ_{eff}, which is defined as

$$\sigma_{\text{eff}}=\sqrt{\tau^2+\sigma^2} \tag{10}$$

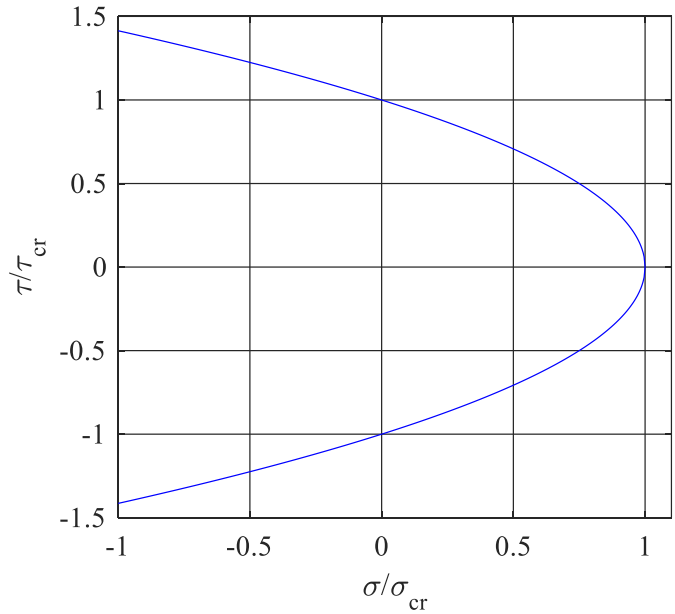

Figure 25. Shape of the fracture criterion.

This definition is illustrated by Figure 26. Similar definition is used in other cohesive formulations for example in models by Höberg (2006) and Camacho & Ortiz (1996). Using this definition the fracture criterion can be written as

$$\frac{\sigma_{eff} \cdot \sin\alpha}{\sigma_{cr}} + \frac{{\sigma_{eff}}^2 \cdot \cos^2\alpha}{{\tau_{cr}}^2} - 1 < 0, \tag{11}$$

where α is the angle between effective stress and shear stress also illustrated in Figure 26. In case of pure tensile stress the effective stress magnitude is equal to the normal stress component and the angle α has a value of 90°. This means that the cosine term of the fracture criterion turns to zero and the sine term has a value of 1. Therefore the softening starts when the effective stress is equal to the critical normal stress as happens with the original form of the criterion. Similarly, in case of pure shear ($\alpha=0$) the effective stress is equal to the shear stress component. This means that the softening starts when the effective stress reaches the critical shear stress value. This is again similar to the original form of the failure criterion.

On the yield surface the effective stress can be solved from Equation (11) which is a standard quadratic equation. According to Equation (10), σ_{eff} must have value $\sigma_{eff} > 0$, so only the positive root is considered. The solution is

$$\sigma_{eff}(\alpha) = \frac{-\frac{\sin\alpha}{\sigma_{cr}} + \sqrt{(\frac{\sin\alpha}{\sigma_{cr}})^2 + 4\frac{\cos^2\alpha}{{\tau_{cr}}^2}}}{2\frac{\cos^2\alpha}{{\tau_{cr}}^2}} \tag{12}$$

As this equation shows, the σ_{eff} on yield surface depends on the load direction α (see Figure 26). The value of σ_{eff} at the yield surface corresponding to a selected α is in the following referred to with symbol σ_{cre} and is called effective critical stress. This means that the softening starts when $\sigma_{eff} \geq \sigma_{cre}(\alpha)$.

In the FEM-DEM simulation the FEM-stage gives the total strain of the element to the fracture algorithm. This means that the total strain can be assumed to be always known. The

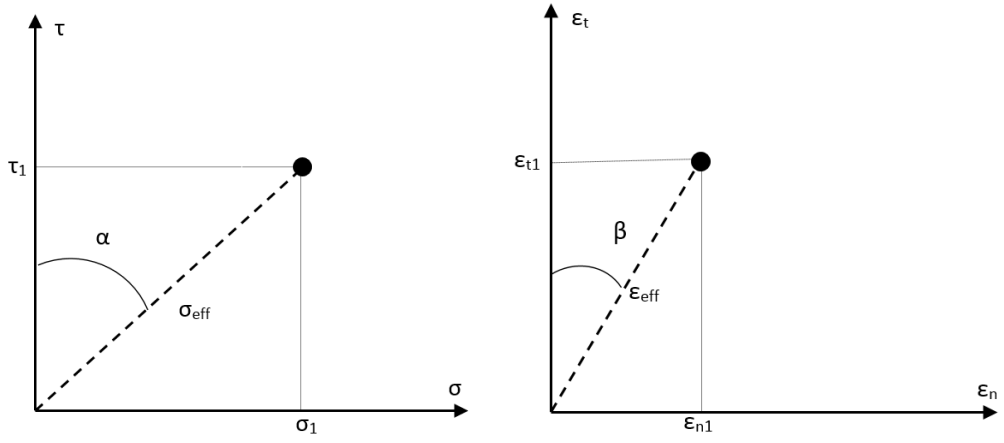

(a) (b)

Figure 26. Definition for effective stress and displacement as well as angles α and β.

total strain has elastic and inelastic components. The inelastic component is due to softening, which leads to non-linear behavior of the element. The stress-strain curve for the model is shown in Figure 27. Before the fracture criterion is reached the response is linearly elastic which is presented in the stress-strain curve between point 0 and A in Figure 27 a. At point A the stress state reaches the critical stress and the softening starts, which leads to the strain having elastic and inelastic components ε^{el} and ε^{f}. The softening happens between points A and C. At point C the crack has fully opened.

The total strain of the beam element after the peak is therefore given by

$$\varepsilon = \varepsilon^{el} + \varepsilon^{f} \tag{13}$$

Since the total strain is always known, it is used to calculate the stress state of the cohesive element. Therefore similarly to the effective stress, an effective strain needs to be defined to reduce the strain state to one dimensional case. The strain has tangential and normal strain components. Effective strain is defined here using these two components as

$$\varepsilon_{\text{eff}} = \sqrt{\varepsilon_{\text{t}}^{2} + \varepsilon_{\text{n}}^{2}}, \tag{14}$$

where ε_t is the tangential strain and ε_n is the normal strain. The definition is illustrated in Figure 26. This means that ε_n presents mode-I opening of the crack and ε_t mode-II opening.

The elastic component of the total strain follows Hooke's law. This means that effective stiffness must be defined for the conversion of effective strain to effective stress. The relation between stress and strain components is defined as

$$\varepsilon_{\text{t}} = \frac{\sigma}{E}, \qquad \varepsilon_{\text{n}} = \frac{\tau}{G_s}, \qquad \varepsilon_{\text{eff}} = \frac{\sigma_{eff}}{E_e}, \tag{15}$$

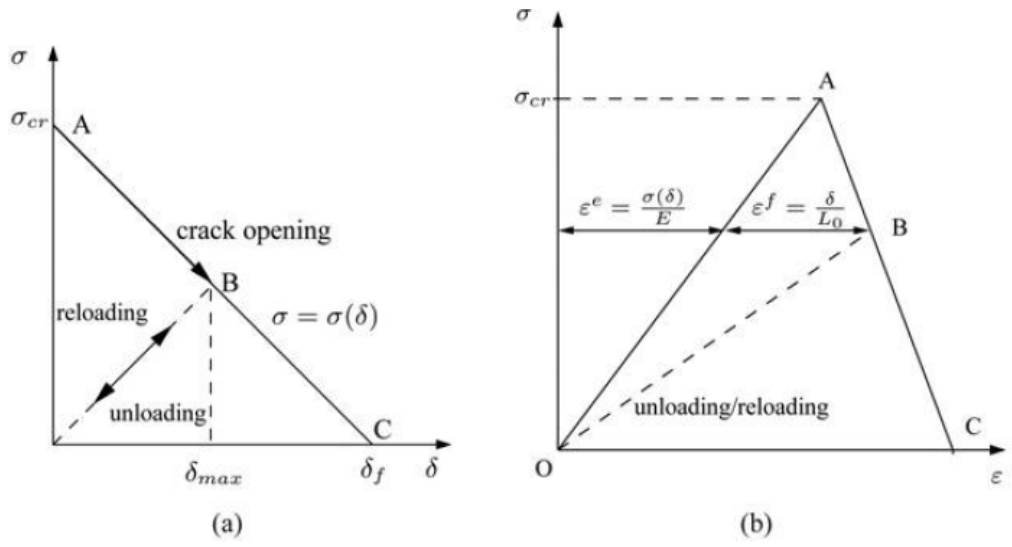

Figure 27. Cohesive behavior of the model (a) and the total response of the model (b). The crack initiates at point A and is fully damaged at point C. (Paavilainen et al., 2009)

where E is Young's modulus, G_s is shear modulus and E_e is the effective Young's modulus. The effective stiffness is obtained by substituting previous equations into Equation (14). This gives

$$\frac{\sigma_{eff}}{E_e} = \sqrt{(\frac{\sigma}{E})^2 + (\frac{\tau}{G_s})^2} \tag{16}$$

From this the effective stiffness E_e can be solved, and it is

$$\frac{1}{E_e} = \sqrt{(\frac{\sigma}{E \cdot \sigma_{eff}})^2 + (\frac{\tau}{G_s \cdot \sigma_{eff}})^2} \tag{17}$$

$$E_e(\alpha) = \frac{1}{\sqrt{\left(\frac{\sin\alpha}{E}\right)^2 + \left(\frac{\cos\alpha}{G_s}\right)^2}}, \tag{18}$$

where α is the angle between effective stress and shear stress component as presented in Figure 26. Using the newly defined effective Young's modulus the elastic strain component is

$$\varepsilon^{el} = \frac{\sigma_{eff}}{E_e} \tag{19}$$

Inelastic strain ε^f represents the crack opening and is defined as

$$\varepsilon^f = \frac{\delta}{L_0} \tag{20}$$

Where δ is the crack opening displacement and L_0 is the beam element length. Therefore the total strain after the softening has started is equal to

$$\varepsilon_{eff} = \varepsilon^e + \varepsilon^f = \frac{\sigma_{eff}}{E_e(\alpha)} + \frac{\delta}{L_0} \tag{21}$$

4.2 Softening behavior

The fracture criterion also needs to account for the previous crack opening. The full form of the Schreyer fracture criterion is

$$F(\sigma, \tau, \delta_{max}) = \frac{\sigma}{\sigma_{cr}} + \frac{\tau^2}{{\tau_{cr}}^2} + \frac{\delta_{max}}{\delta_f} - 1 < 0, \tag{22}$$

where δ_{max} is the maximum achieved crack opening displacement and δ_f is the critical crack opening displacement. Using the newly defined effective critical stress σ_{cre} the fracture criterion can be formulated into

$$F(\alpha, \delta_{max}) = \sigma_{eff} - \sigma_{cre}(\alpha)[1 - \frac{\delta_{max}}{\delta_f}] \quad (23)$$

When σ_{eff} reaches this value, the softening of the cohesive element starts. To check that both criterions presented in Equations (22) and (23) define the same yield surface, effective stress at which $F=0$ according to Equation (22) and the effective critical stress in the corresponding loading direction are calculated. The difference between these two stresses is observed to be zero with all angles. The effective critical stress can also be plotted in polar coordinates as a function of α. This is plotted in Figure 28, and shows that the graph has similar shape as the undamaged fracture criterion plotted in Figure 29. These graphs show that the use of effective stress and effective critical stress results in fracture occurring at similar stress states.

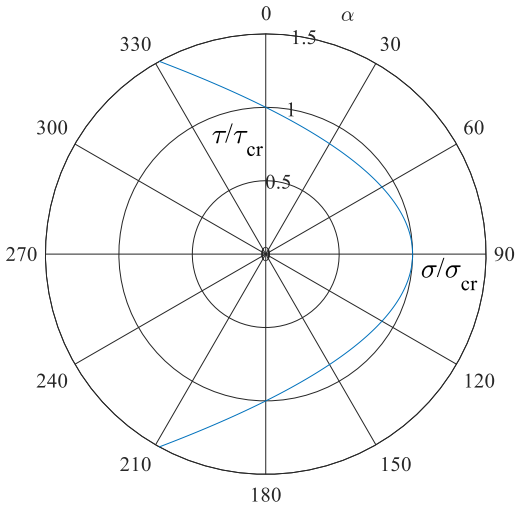

Figure 28. Effective critical stress plotted into polar coordinate system as a function of α. The shape is identical to the original yield surface, which is plotted on the figure using orange dots.

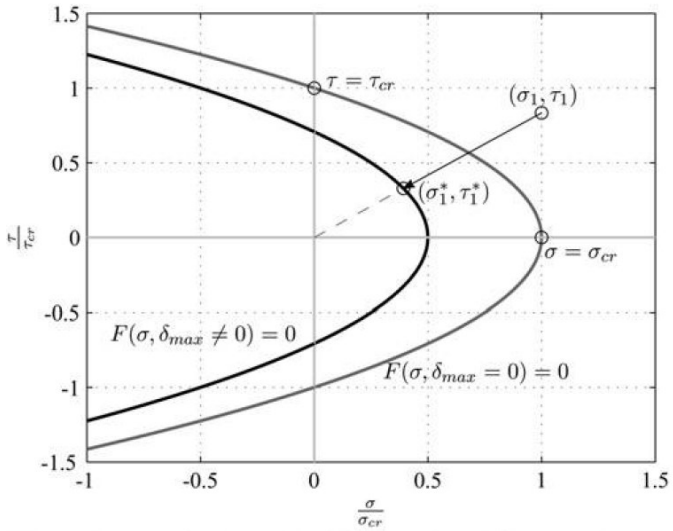

Figure 29. Example of how the return mapping adjusts the fracture surface. The figure shows the original fracture surface. (Paavilainen et al., 2009)

In short, fracture criterion has the following practical meaning: When $F<0$, the stress state is admissible and the crack does not open. Stress states in which $F>0$ are not admissible and in such cases the stress state needs to be returned to the yield surface where $F=0$ using a return mapping algorithm similar to one presented by Simo & Hughes (1998) for plasticity. This means that the crack is propagating when $F=0$. The return mapping is done in a way that preserves the relation between normal and shear stresses. An example of return mapping is presented in Figure 29. The return mapping works as follows: When the stress state exceeds the fracture criterion, a new δ is calculated as described below. A new stress state is then calculated using the new δ according to the softening function.

To achieve the above described behavior, first the fracture criterion is checked using a trial stress at each step during the simulation. The trial stress is calculated from Equation (21)

$$\sigma_{k+1}^{trial} = E_{eff}(\alpha) \cdot \left(\varepsilon_{k+1} - \frac{\delta_{max}^{k}}{L_0} \right), \tag{24}$$

where the subscript k refers to previous step and $k+1$ is the current step.

The model uses linear softening function. During the softening a new value of cohesive stress needs to be defined as a part of the return mapping algorithm. The cohesive stress that acts over the crack during softening is defined as

$$\sigma_{eff} = \sigma_{cre}(\alpha)[1 - \frac{\delta}{\delta_f}] \tag{25}$$

The cohesive stress reduced linearly as a function of δ_{max} as was defined when selecting the softening function. The δ is always the δ_{max} due to when the cohesive softening is active. New value for crack opening needs to be solved to calculate the cohesive stress on the new fracture surface. This can be solved from Equation (21) as the total strain is known, by substituting the cohesive stress into the equation. This results in following

$$\varepsilon_{eff} = \frac{\sigma_{cre} \cdot (1 - \frac{\delta}{\delta_f})}{E_e} + \frac{\delta}{L_0} \tag{26}$$

From this equation δ can be solved

$$\varepsilon_{eff} - \frac{\sigma_{cre}}{E_e} = (-\frac{\sigma_{cre}}{E_e \delta_{cr}} + \frac{1}{L_0})\delta \tag{27}$$

$$\delta = \frac{\varepsilon_{eff} E_e - \sigma_{cre}}{\frac{E_e}{L_0} - \frac{\sigma_{cre}}{\delta_f}} \tag{28}$$

The new δ is then used to calculate corresponding cohesive stress σ_{eff} using Equation (25). Critical COD is defined using fracture energy and critical stress as mentioned in chapter 2. With linear softening function, the formula is

$$\delta_f(\alpha) = \frac{2G_f}{\sigma_{cre}(\alpha)}, \tag{29}$$

where G_f is the fracture energy per unit area. The δ_{cr} depends on effective critical stress, which in turn depends on the angle α. This results in the δ_{cr} direction and magnitude changing as a function of α. The model needs to use scalar COD variable to keep track of the previous opening in cases where the direction of loading change between steps, to ensure that the ratio δ_{max}/δ_f stays constant regardless of the load direction change. The scalar COD variable is defined as δ_{max}/δ_f, which is used to transfer the magnitude of δ_{max} between iteration steps. At the start each iteration step the current δ_{max} obtained by multiplying the scalar COD value with the current δ_f.

The model can experience unloading after the crack has formed when F<0. This handled using unloading-reloading part of the model. During unloading crack propagation stops and the crack starts to close, as demonstrated between points B and O in Figure 27. Previous δ_{max} does not decrease however. The stress acting over the crack varies linearly depending on the crack closure or opening. The cohesive stress acting over the crack is calculated similarly as in Equation (25), but it is multiplied by the ratio between current crack opening and previous maximum crack opening. The resulting equation is

$$\sigma_{eff} = \sigma_{cre}\left(1 - \frac{\delta}{\delta_f}\right)\frac{\delta}{\delta_{max}}, \tag{30}$$

where δ is the current crack opening calculated from Equation (28), which is less than the δ_{max}. When $\delta=\delta_{max}$, the Equation (30) turns into Equation (25) and the softening continues.

At the end of the softening algorithm the effective stress is returned back to two dimensional state. This is done using the definition of effective stress demonstrated in Figure 26. This ensures that the relation between τ and σ does not change during the softening process.

4.3 Critical element length

The value for δ needs to be positive. After the softening has started the numerator part of Equation (28) is always positive. This means that the denominator of Equation (28) needs to be positive. This defines the maximum element length for the beam element. The maximum element length can be solved from the denominator of Equation (28) as follows:

$$\frac{E_e}{L_0} - \frac{\sigma_{cre}}{\delta_f} > 0 \tag{31}$$

$$L_0 < \frac{E_e \delta_f}{\sigma_{cre}} \tag{32}$$

By substituting δ_{cr} from Equation (29) to the equation the final form for maximum element length is obtained

$$L_0 < \frac{2E_e G_f}{{\sigma_{cre}}^2} \tag{33}$$

The σ_{cre} depends on the angle α, which means that the maximum element length varies with different loading direction. The maximum element length decreases as the value of σ_{cre} increases, which happens when the amount of compressive load increases. The minimum element length is governed by simulation time. Smaller beam element lead to larger amount of elements in the Aalto FEM-DEM code, which in turn decreases the calculation time.

4.4 Energy dissipation

The total energy dissipated is defined to be the sum of the energy dissipated by the two modes. This energy is also equal to the value dissipated by the effective displacement. This means that

$$G_f = G_I + G_{II} = G_e, \tag{34}$$

where G_I and G_{II} are the energies dissipated by the two different modes and G_e is the energy dissipated by the effective displacement. This results from the definition of effective critical stress and critical COD. The integrations are done according to Equation (1) as follows

$$G_I = \int \sigma(\delta_n) d\delta_n = \int L_0 \cdot \sigma(\varepsilon_n) d\varepsilon_n \tag{35}$$

$$G_{II} = \int \tau(\delta_t) d\delta_t = \int L_0 \cdot \tau(\varepsilon_t) d\varepsilon_t \tag{36}$$

$$G_e = \int \sigma_e(\delta_e) d\delta_e = \int L_0 \cdot \sigma_e(\varepsilon_{eff}) d\varepsilon_{eff}, \tag{37}$$

where the subscript *n* refers to normal component, *t* to tangential and *e* to effective direction.

A flowchart for the new model is presented in Figure 30 to further clarify the operation and how it is connected to the FEM-DEM code. The most important changes are the new definition of effective stress which results in a new definition of effective critical stress. Other changes result from these two changes. Overall the changes should lead to better behavior in shear dominated cases. When no stress is transmitted through the cohesive elements, the crack has fully propagated through the beam element. This leads to the separation of the connected discrete elements.

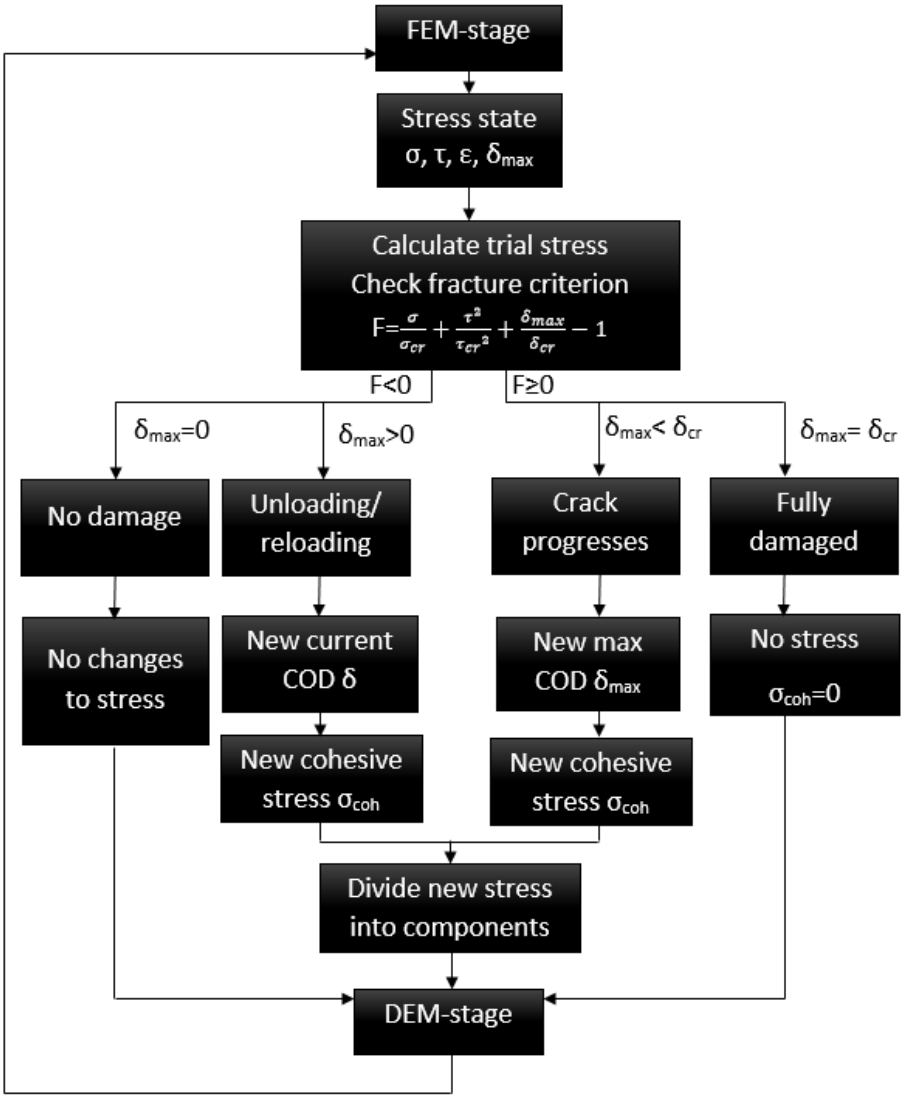

Figure 30. Flow chart for the new model. It shows how the model works and how it is related to the rest of the simulation when implemented into the FEM-DEM simulation code.

4.5 Implementation to MATLAB

The new cohesive crack model is implemented into MATLAB as a function. Separate test script is created to test its behavior to see if it provides better results compared to the previous one. The cohesive crack algorithm and an example test script are included in Appendix 1 and 2 respectively. The test script uses forced displacement to load the model. Dissipated energy is then calculated from the test data to see if it matches the value given as a material parameter. A flow chart of the test script behavior is presented in Figure 31. Different variables that are transferred between the test script and the cohesive crack algorithm are listed in Table 7. The variables given to the algorithm are also presented in Figure 31.

The forced displacement algorithm works as follows: A displacement vector that holds the x and y coordinates for each displacement step is created. The cohesive crack model is

Table 7. The parameters transferred between the test script and the cohesive crack algorithm.

Parameters given to the algorithm		Parameters the algorithm returns	
Displacement components	u_t & u_n	Effective stress	σ_e
Damage scalar variable	δ_{max}/δ_{cr}	Effective strain	ε_e
Element length	L_0	Fracture criterion variable	F
Elastic modulus	E	Damage scalar variable	δ_{max}/δ_{cr}
Shear modulus	G_s	Current crack opening ratio	δ/δ_{cr}
Fracture energy	G_f	Stress components	σ_n & τ_t
Critical stress components	σ_{cr} & τ_{cr}	Strain components	ε_n & ε_t
Element status variable	st	Element status variable	st

Table 8. Different energies calculated by the test script. Subscripts l and f stand for elastic and inelastic, and t, n and e stand for tangential, normal and effective.

Energy	Stress	Displacement
G_I	σ	$\varepsilon_n L_0$
G_{II}	τ	$\varepsilon_t L_0$
G_e	σ_e	$\varepsilon_e L_0$
$G_{I\,\delta}$	σ	δ_n
$G_{II\,\delta}$	τ	δ_t
$G_{e\,\delta}$	σ_e	δ_e

Table 9. Parameters required by the model and their values.

Parameter (symbol)	Unit	Value
Critical normal stress (σ_{cr})	kPa	540
Critical shear stress (τ_{cr})	kPa	725
Fracture energy (G_f)	J/m^2	15
Element length (L_0)	m	0,03
Young's modulus (E)	GPa	4
Poisson's ratio (v)	-	0.3
Number of steps (n)	-	500

applied at each step. The stress state is generated from the used displacement step. The results from the cohesive crack model are then saved for further analysis. After this, new step starts. Procedure is repeated until $\delta=\delta_{cr}$. The energy dissipated is integrated from both total strain and the crack opening as presented in Equations (35) to (37). The different energies listed in Table 8 are calculated from the simulation data busing tools provided by MATLAB. Total strain used consists of elastic and inelastic components as stated in Equation (13).

The test script requires several parameters as input. These include the forced displacement vector and the material parameters listed in Table 9. The values for the material parameters are selected according to Timco & Weeks (2009). In addition to the material parameters the number of steps used in the forced displacement test is required. The displacement vector can be created by selecting a maximum forced displacement length, and then dividing it to the selected number of steps.

The test script includes two different test types. First test is mixed-mode energy test. The aim of this test is to check if the model dissipates the correct amount of energy in every loading direction. In this test the displacement test is repeated with the direction of forced

displacement varying from pure tangential displacement to pure normal direction. The angle used in the results is the angle β presented in Figure 26. Each of these tests is done separately and dissipated energy is then calculated after each loading direction. This is similar test to what was used to present the problems in the original model earlier in this chapter. For this test the displacement vector is slightly longer than the maximum critical crack length to ensure that the element will be fully damaged after the test.

Second test performs a single test that loads the element first in one direction, then unloads it followed by displacement in new direction. This test is used to test the unload-reload

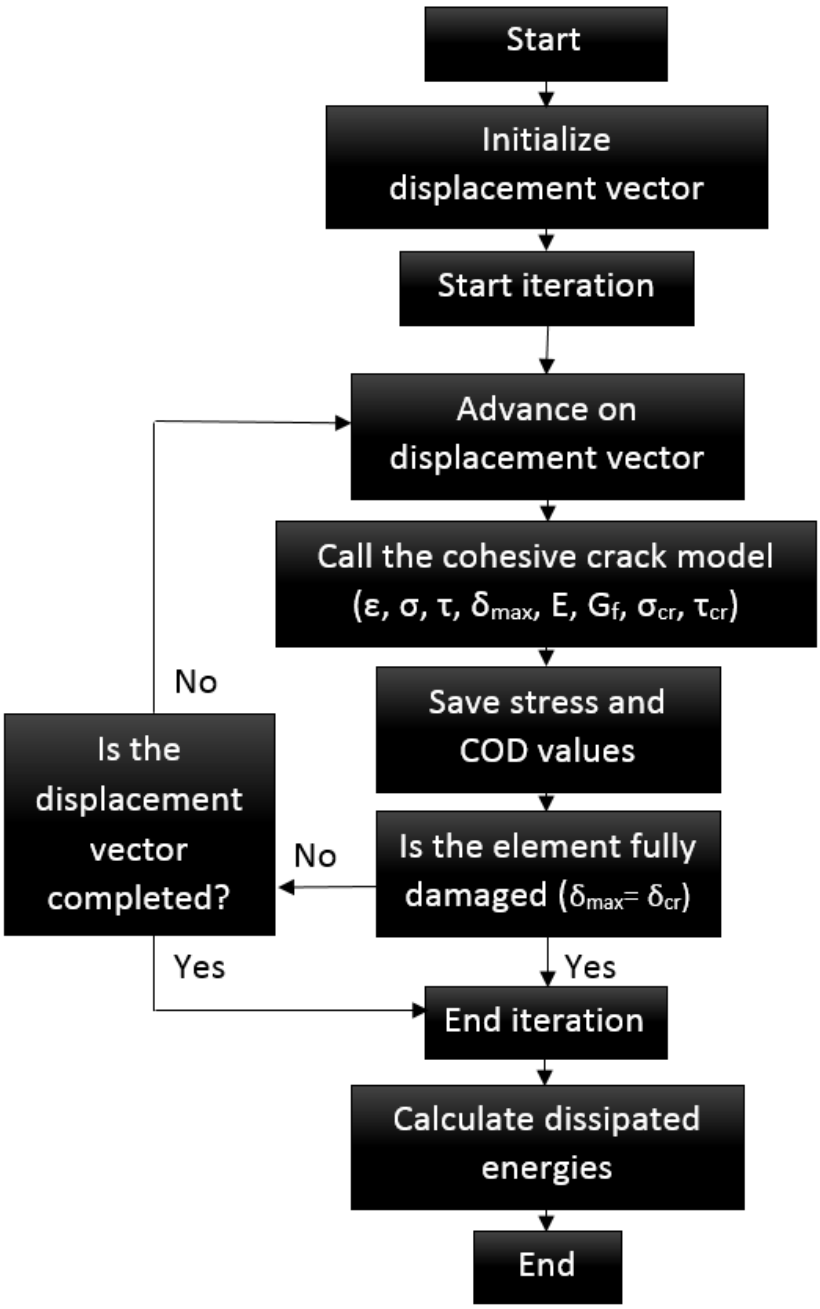

Figure 31. Flowchart of the test script. Symbols inside brackets show what parameters are either transferred or used

behavior as well as load changing behavior. Additionally the test can be done without the unloading part, which means that the direction of the forced displacement changes during the softening.

As stated earlier, the model becomes unstable when the selected beam element length is too large. This is controlled by an error check that warns the user when the model uses too large element length. The check is similar to the one presented in Equation (33). The check is done in the beginning of the test algorithm using the two critical stress components.

5 Results and Analysis

The above presented model was validated using MATLAB. Different test cases were used to test the new model and compare its performance to the original model. In this chapter the general behavior of the model is inspected first, with forced displacement in normal and tangential directions. This is followed by a mixed-mode case. After these a wider mixed-mode test is used to validate the mixed-mode performance in other directions. Unloading and reloading behavior is tested with a case where the load drops to zero during unloading, as well as with a case where it does not. Finally the effect of the used displacement step and the maximum element length are studied. The results are followed by analysis on the model behavior along with a discussion on its limitation.

A schematic of the forced displacement tests is presented in Figure 32, where u_e is the total forced displacement, and u_n and u_t are the normal and tangential displacement components. Angle β is the angle between the effective and tangential displacement. This means that β = 0° when the displacement is tangential to the fracture plane, and β = 90° when normal to the fracture plane. The components and the angle β are defined similarly to the strain components in Figure 26 b. The element length (L_0) in most of the tests was $3 \cdot 10^{-2}$ mm, as stated in Table 9.

5.1 Pure tensile and pure shear cases

The general behavior of the model was tested by loading the model in pure tension and pure shear until crack had fully opened. The behavior of the new model was compared to the MATLAB implementation of the original model. All of the used material parameters and their values are listed in Table 9. The energy dissipated in all cases should be 15 J.

First the model was tested in pure tensile loading. This is the direction in which the original model worked correctly. In this case the maximum stress at which the softening starts is equal to the critical normal stress, which has a value of 540 kPa (σ_{cr} in Table 9). The critical

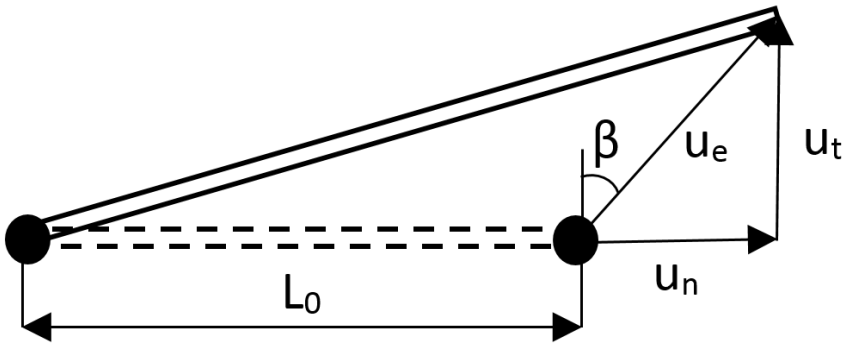

Figure 32. Schematic of the forced displacement test. In the figure a beam element with initial length L_0 is subjected to forced displacement of magnitude u_e to direction β (Same as in Figure 26 b). The cohesive crack model is applied in the middle of this beam. The displacement has tangential (u_t) and normal (u_n) components. Dashed lines represent the initial length of the beam.

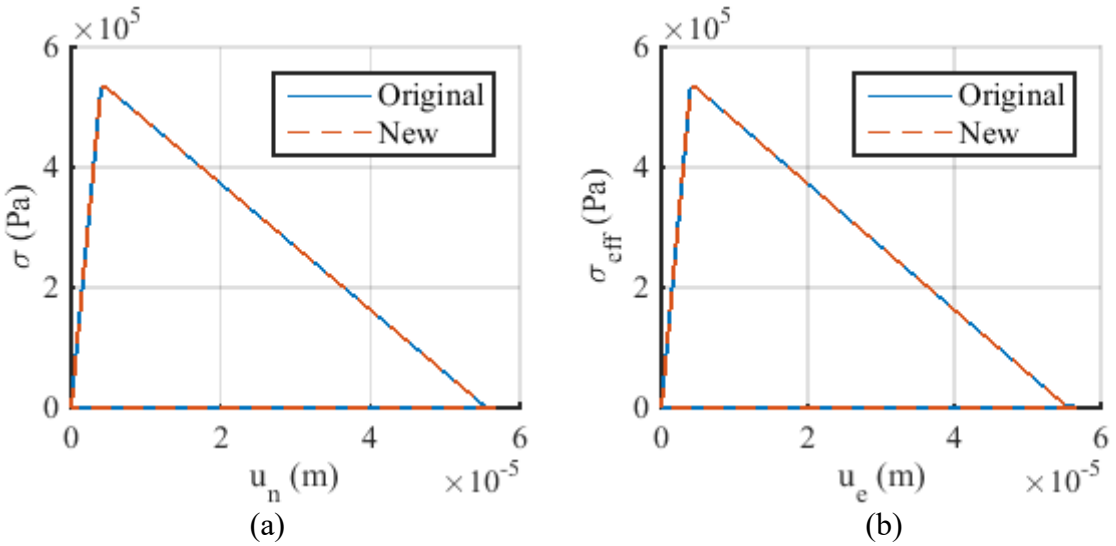

Figure 33. Stress-displacement figures of pure tensile loading case. (a) shows the normal stress-displacement and (b) effective stress-displacement behavior. The graphs are identical. u_n is the normal direction displacement component and u_e is the effective forced displacement. In pure tension they are equal.

crack opening (δ_f) is calculated according to Equation (29) and is $5.56 \cdot 10^{-2}$ mm. The stress-displacement (σ-u_n) graphs for both the original and new models are presented in Figure 33 a. Both the original and new models have virtually exactly correct shapes, which shows that the new model works similarly to the original model. Both models dissipated almost correct amount of energy, the error being very small, only $3 \cdot 10^{-3}$ %. The softening started at σ = 539.1 kPa and the maximum δ is $5.56 \cdot 10^{-2}$ mm in both the original and new model. At the time of final fracture in the new model $\delta = u_n$.

Further Figure 33 b shows an effective stress-displacement (σ_{eff} - u_e) record for the tensile case. In pure tensile case the following equations are satisfied: $\sigma = \sigma_{eff}$ and $u_n = u_e$. The figure has similar shape and the dissipated energy as well as maximum σ_{eff} and δ have same values as in the component graph. This means that both models work correctly and identically when loaded in pure tension.

The small differences in the values of fracture energy, maximum σ and final δ obtained from the new model to their theoretical values were small. The difference resulted from the numerical procedure used in the model and from the selected displacement step length, which also defines the smallest change in stress. This means that the stress could not reach the exact critical stress value, before the softening started. Similar behavior was observed with maximum crack opening displacement (COD). By decreasing the displacement step size the error decreased. Therefore the minor error in the values is not important. The selected element size (L_0 = 0.03 m) was much smaller than the critical element length, which with selected material parameters is 0.247 m (Equation (33)).

Similar test was conducted for pure shear case. As stated earlier, this is the mode in which the original model does not behave correctly. In pure shear the critical shear stress is 725 kPa (τ_{cr} in Table 9), and the δ_f is $4.14 \cdot 10^{-2}$ mm calculated from Equation (29). Similar graphs to those used in previous tests are presented in Figure 34 a and b. The Figure 34 a shows that the new model behaves quite differently compared to the original model. While the

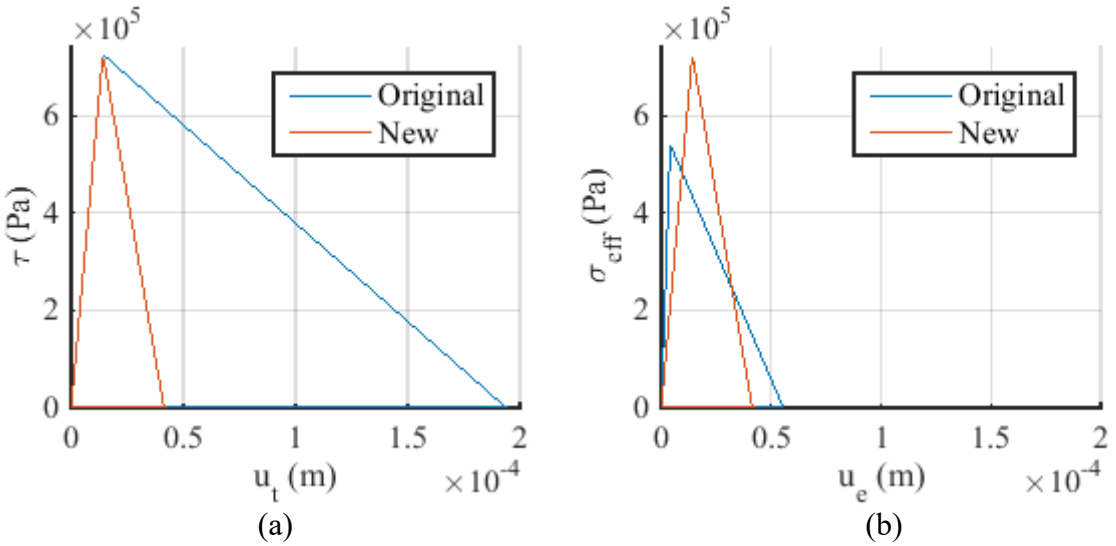

Figure 34. Stress-displacement figures of pure shear loading case. (a) shows the tangential stress-displacement ($\tau - u_t$) and (b) shows the σ_{eff} - u_e behavior. The graphs show the different behavior between the original and new models. u_t is the tangential direction displacement component and u_e is the effective forced displacement. In pure shear they are equal in the new model.

maximum obtained stresses were close to each other, the values of maximum δ were different. The δ value for the new model gave the correct value, while the original model achieved maximum opening of $1.95 \cdot 10^{-1}$ mm which is 4.6 times higher than the intended value. The dissipated energies by the two models were 15 J and 70.3 J for the new and original model respectively. The original model dissipated too much energy. When the dissipated energy was calculated from the σ_{eff} - u_e graph shown in Figure 34 b, both models dissipated correct amount of energy. The values for dissipated energy obtained from the component graph and the effective graph should be equal in the new model, as is the case ($\tau = \sigma_{eff}$ and $u_t = u_e$.). In Figure 34 b the graph created from original and new models are quite different. The elastic behavior of the original model is much steeper compared to the new model, and the maximum stress obtained by the original model is equal to the critical normal stress value. Both of these features are intended in the formulation of the original model, and are not errors.

5.2 Mixed mode test

Mixed-mode behavior test loaded the element in angle $\beta = 10°$ (see Figure 26 b). Due to the difference between the values of Young's modulus and shear modulus the stress acts in angle $\alpha = 24.6°$ (see Figure 26 a). The value of σ_{cre} according to Equation (12) in the corresponding direction is 589 kPa and the corresponding δ_f according to Equation (29) is 5.09 10^{-2} mm. The component values are as follows: the maximum normal stress is 245 kPa and maximum shear stress is 535 kPa. Similarly the value of maximum COD in normal direction should be $0.88 \cdot 10^{-2}$ mm and $5.02 \cdot 10^{-2}$ mm in tangential direction.

The resulting σ_{eff} - u_e graph for both the original and new model is plotted in Figure 35. The values for dissipated energy as well as maximum COD values for both models are presented in Table 10. The total dissipated energy by both the new model and old model calculated

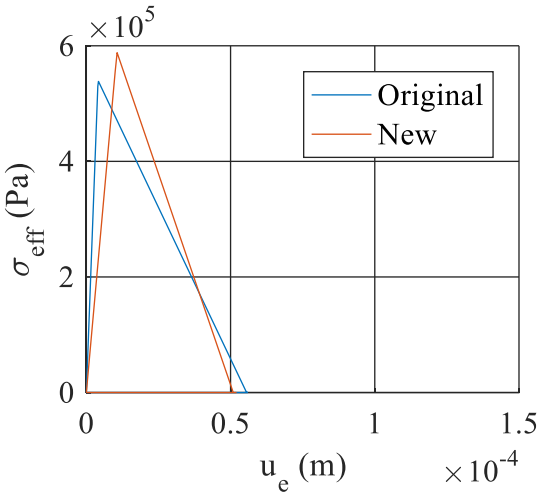

Figure 35. σ_{eff}-u_e figure of mixed-mode case. The graph shows the difference between the behavior of original and new models.

from σ_{eff}- u_e data was 15.0 J. Similarly the energy dissipated can be integrated from the stress components and summed. This gave the new model dissipated energy a value of 15.0 J, while the old model dissipated 48.9 J, which is higher than intended. This value is closer to the correct value than the value obtained in pure shear case. The difference is due to the fracture occurring at much higher displacements than intended, as is observed in the pure shear case. The fracture initiates at correct stress.

The models were also compared using effective stress-COD (σ_{eff}-δ) graph, which is plotted in Figure 36 for the mixed-mode case. The shape of the graph differs from the previous ones by not having the initial elastic part. This shows that no crack opening displacement is present before the softening starts and that the model has extrinsic behavior as intended. The maximum values for σ_{eff} and δ for both models are similar to those in Figure 35.

Table 10. Results of the mixed-mode test. The table includes the values from the new and original models, as well as the values they should be according to the equations presented in this work. Each model gives effective values as well as its component values.

		G [J]	δ_{max} [10^{-2} mm]
New	Effective	15.00	5.20
	Normal	2.61	0.903
	Shear	12.39	5.12
Original	Effective	15.00	5.59
	Normal	4.12	2.93
	Shear	50.98	16.6
Correct	Effective	15	5.09
	Normal	2.60	0.88
	Shear	12.40	5.02

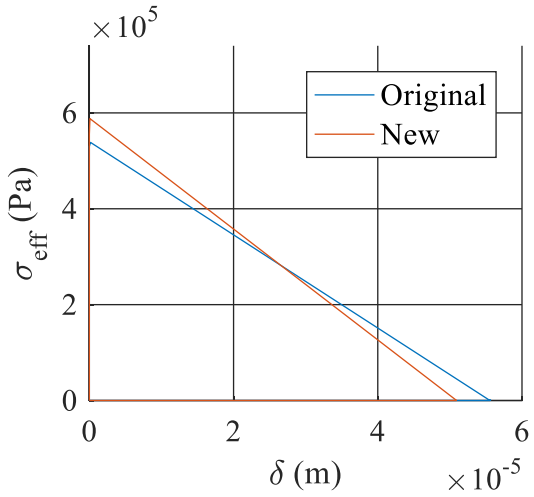

Figure 36. Stress-COD (σ_{eff}-δ) figure of the mixed-mode case. The figure shows that behavior of both original and new models is extrinsic.

As demonstrated with the three test cases, the new model gives correct dissipated energy values, while the original model dissipated too much energy in other cases than pure tensile loading. The different stress-displacement figures of the new model have correct shapes. The linearly elastic part of the beam element is followed by linear softening. The σ_{eff}-δ figure shows that the cohesive behavior is extrinsic since no COD is observed prior to the critical stress.

The original model dissipates wrong amount of energy, since the maximum COD values are much higher than the values they should have. The main differences result from the formulation of effective strain, which is then used to calculate effective stress. This causes the final fracture to occur at much larger displacement values in shear dominated cases. The difference between the shapes of the original and new σ_{eff}-u_e graphs is due to the original model using only normal direction material parameters. This is however not an error, but rather a different approach in the model formulation.

5.3 Fracture energy in mixed-mode failure

As stated above, the goal of this work was to derive an extrinsic cohesive element, which dissipates correct amount of energy independent of the fracture mode. To demonstrate this feature a numerical experiment, in which the element was loaded using a monotonously increasing displacement with varying angle in relation to pure shear. Angels between 0° and 90° were tested.

Figure 37 presents the different dissipated energy values for the new model, and Figure 38 shows similar values from the original model. The largest difference between the original and the new graphs is that the total energy dissipated in the new model was constant 15 J, and that the sum of the energy components was equal to the energy dissipated by the effective opening, which satisfies the relation presented in Equation (36). This means that the model works as intended regardless of the direction.

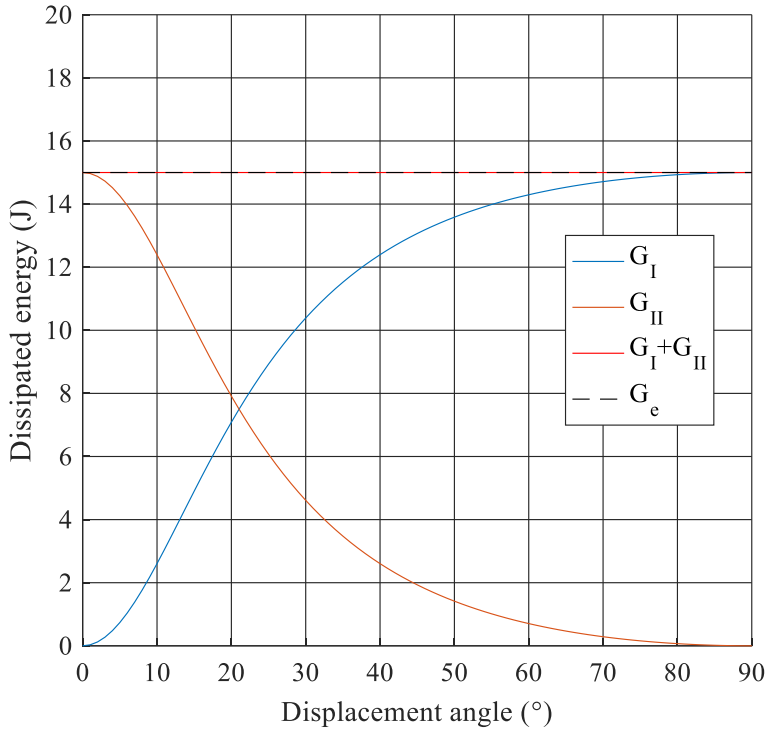

Figure 37. Energy dissipated by the new model with different angles, calculated from the stress-displacement data.

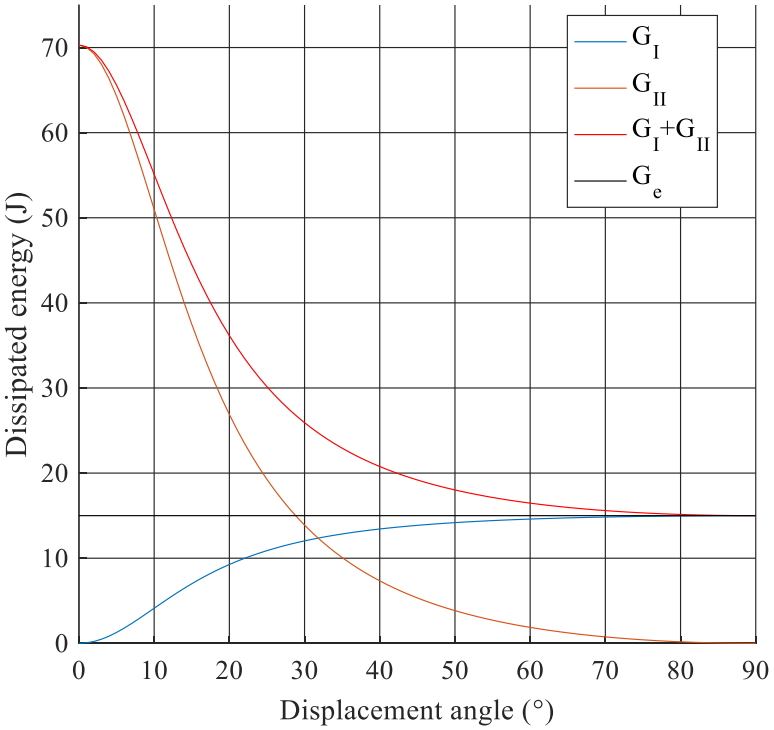

Figure 38. Energy dissipated by the original model with different angles, calculated from the stress-displacement data.

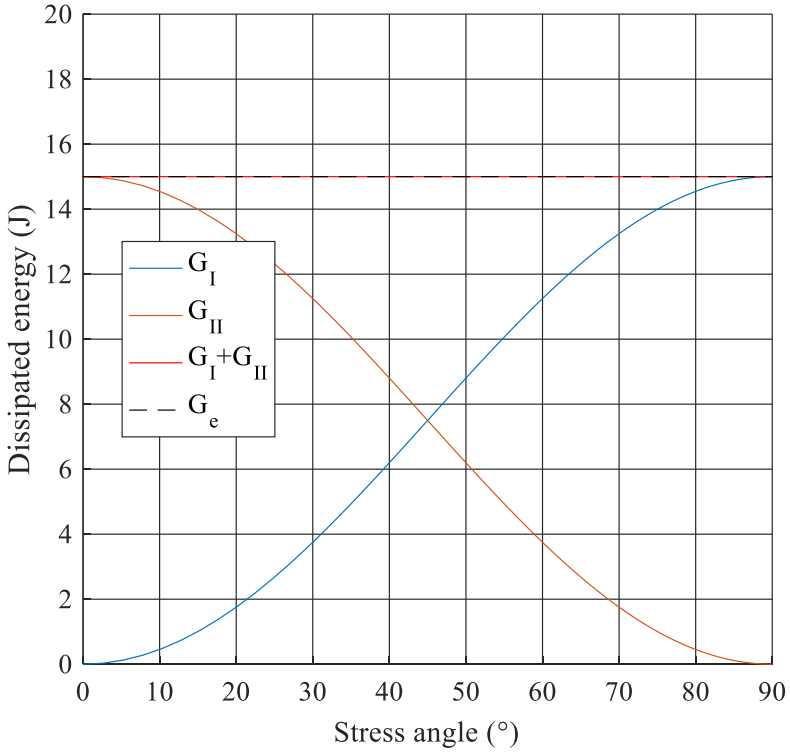

Figure 39. Dissipated energies plotted in respect to the stress angle α, calculated similarly to Figure 26.

The same test was performed to the original model. The resulting graph plotted in Figure 38 is identical to the one that was used to demonstrate the problems of the original model in previous chapter in Figure 24. Additionally to Figure 24, the Figure 38 includes G_e. The amount of energy dissipated was correct in pure tensile case. Immediately after the pure tensile case the total energy dissipated started to increase, first slowly. As the effect of shear stress increased, the error started to increase quite rapidly, until reaching the maximum dissipated energy of 70.3 J at pure shear case. The effective dissipated energy gave the correct amount in all directions, as is expected, since the values of maximum σ_{eff} and δ do not depend on the loading angle.

In Figure 37 the normal stress started to dominate the fracture at $\beta = 21°$. Since the direction of the effective stress α is different to the direction of the effective displacement β as stated in Chapter 4. The dissipated energies are plotted with respect to the stress angle α in Figure 39. In this graph the normal stress component started to dominate the fracture process with $\alpha = 45°$. The large difference between the angles resulted from Young's modulus E being much larger than the shear modulus G.

To ensure that the failure initiates at the correct stress state in the new model, the maximum stress state obtained for each angle was compared to the original fracture criterion given by Equation (9). The original fracture criterion and the maximum stress states are plotted in

Figure 40. The figure shows that the softening in the new model initiates at the original yield surface regardless of the loading direction.

The effect of different material parameters on the error in dissipated energy from both new and old model was also studied. The dissipated energy was calculated from the stress components, and the error percentage was defined as error = $(G_I+G_{II}-G_f)/G_f$. The error in dissipated energy from the new model was very small, and was caused by the numerical scheme. The error of the original model was observed to depend on the value of G as well as the ratio σ_{cr}/τ_{cr}. Young's modulus and the magnitude of critical stress components only had very small effect (< 1 %) on the error, which was caused by the numerical procedure. The error with respect to the displacement angles with different values of G are plotted in Figure 41 - Figure 43. The figures shows that the magnitude of error increased when the fracture procedure started to be shear dominated. Additionally the figure shows that the ratio σ_{cr}/τ_{cr} had the highest influence on the magnitude of error. The error decreases as the ratio approached 1. With the ratio of 1, the magnitude of error was still noticeable. As seen from the figures, G influenced the magnitude of error less, and the magnitude of influence decreases as the ratio approaches 1. None of this was observed with the new model. The previous tests were done with the ratio $\sigma_{cr}/\tau_{cr} \approx 0.75$, which is a good estimate for sea ice (Timco & Weeks 2009)

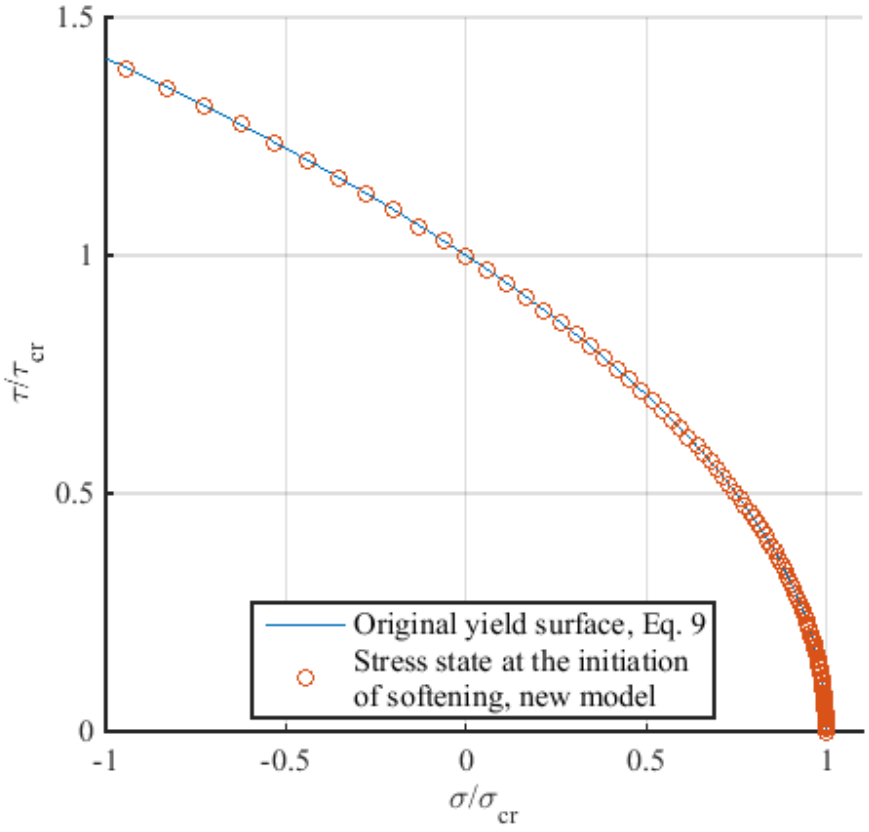

Figure 40. Maximum stress states obtained in the new model compared to original yield surface.

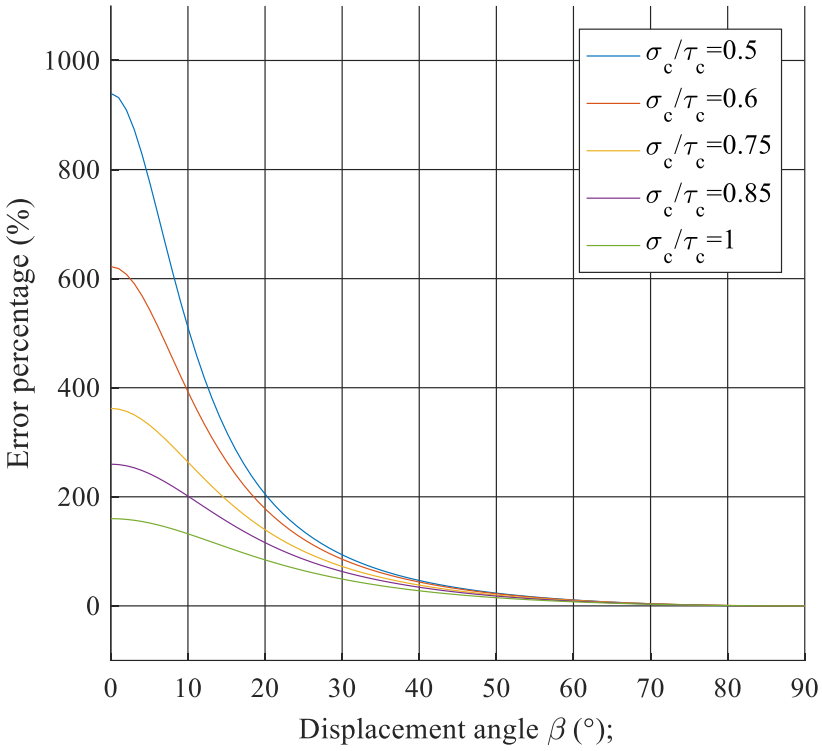

Figure 41. The error percentage in the dissipated energy of the old model with G = 1.54 GPa.

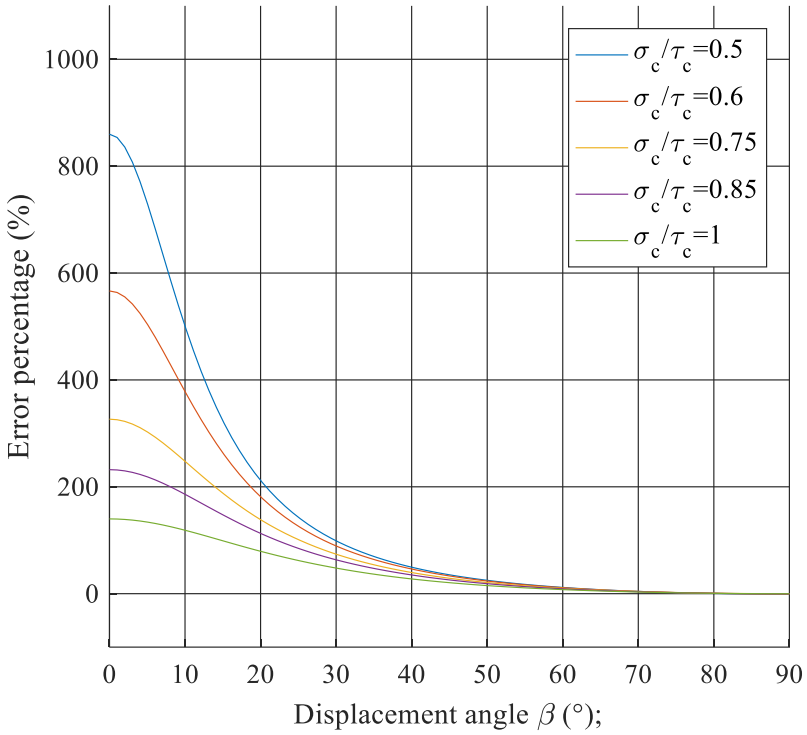

Figure 42. The error percentage in the dissipated energy of the old model with G = 1.76 GPa

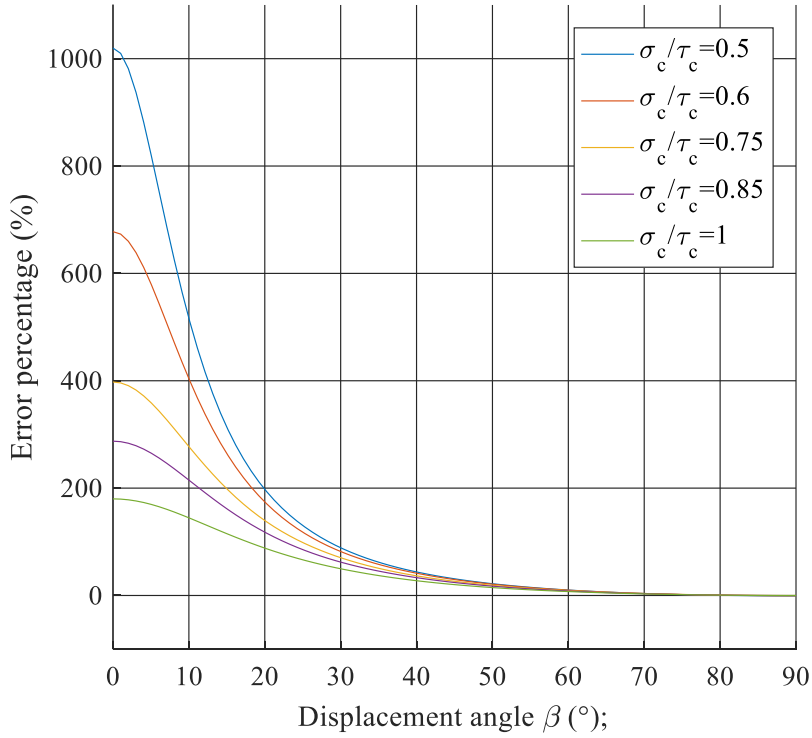

Figure 43. The error percentage in the dissipated energy of the old model with G = 1.43 GPa

The mixed-mode behavior was also investigated with a wider angle range to see if the new model works as intended outside the earlier angle range. The wider angle range ranged from 60° to 240°. This range also included the effect of compression. Due to the shape of the yield surface, the softening cannot start with pure compressive stress. Angles outside this range were not studied, since they would require considerable compression. For this analysis the element length had to be smaller, since under compression the value of critical element length decreases due to it depending on the value of σ_{cre}, which in turn depends on loading direction. At -60° angle L_0 according to Equation (33) was $1.32 \cdot 10^{-2}$ mm which was much smaller than the element length used earlier in this study. A slightly smaller element length than the critical length of $1.25 \cdot 10^{-2}$ mm was used. The original model does not share the varying critical element length property, and did not need a smaller element length.

The results obtained from the new model are plotted in Figure 44 and from the old model in Figure 45. The new model worked well with both positive and negative tangential displacement, which resulted in the dissipated energy figure being symmetric on both sides of the 90° mark. When under high compressive stresses the accuracy started to decrease slightly and total dissipated energy values varied by maximum of 1 %. This was caused by the critical stress rising to very high values, which in turn resulted in very small δ_f. Since the length of the used displacement step is constant regardless of the loading angle while the δ_f decreases, the whole softening process happened in only few displacement steps when under compressive loading as presented in Figure 46, which is created from the 240° displacement data. The blue circles in the figure represent the data points. The small number of data points caused the inaccuracies in dissipated energy. The error could be decreased by using smaller displacement step size. Using too small step size would lead to increased calculation times in non-compressive situation.

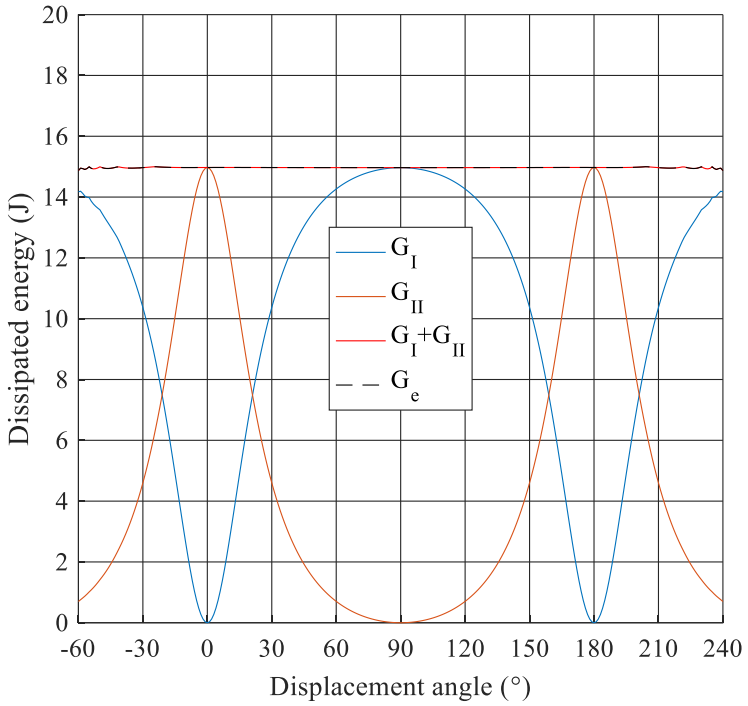

Figure 44. Energy dissipated by the new model with wider angle range. The accuracy is good, with slight reduction at the edges of the angle range. The figure is symmetric on both sides of the 90 degree mark.

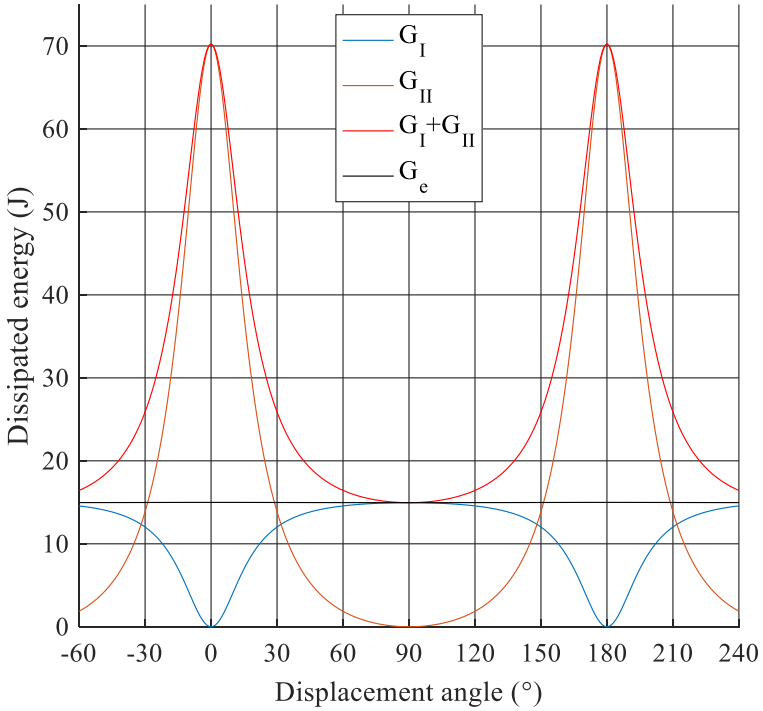

Figure 45. Energy dissipated by the original model with wider angle range. The accuracy is good when tensile stress dominates the fracture process. Biggest error occurs under pure shear loading.

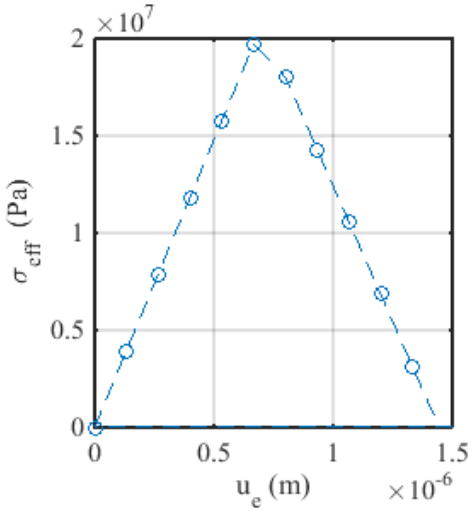

Figure 46. σ_{eff} - u_e graph in 240° direction. Here the blue dots are the data points obtained from the simulation. At high compressive stresses the fracture occurs with only a few displacement steps.

Similar graphs for the original model are presented in Figure 45. This graph is also symmetric across the 90° mark. The element length used is the same as in previous test (0.125 mm). The inaccuracies that were observed in Figure 44 were again present when mode-II was the dominating fracture mode, at around 0° and 180° marks. When mode-I dominated the fracture, the dissipated energy was closer to the correct value. This happened also when the compressive stress started to be the dominating stress component. Second big difference to the new model is that no decrease in accuracy was observed when moving to very high compressive stresses. The reason for this lies in again in the critical stress definition. Since the critical stress had the same value regardless of the loading angle, the amount of steps it takes to reach the maximum COD stayed the same. The effect presented in Figure 46 was therefore not observed.

5.4 Mixed-mode fracture with un- and reloading

The unload-reload relationship was tested using a displacement sequences which first loads the model in one direction, after which it unloads to $u_e = 0$, and reloads the model again in a new direction. A total of five different sequences were used and they are listed in Table 11. The angles represent the angle β. The sequences were chosen to change the fracture mode during the reloading process. The dissipated energies for each sequence by both the old and new model are listed in Table 12. The new model dissipated correct amount of energy with all of the vectors, while the old model dissipated the wrong amount of energy, when the energy is calculated from the stress components.

The results can be illustrated using a normalized stress-displacement curve ($\sigma_{eff}/\sigma_{cre}$ - u_e/δ_f). This is done to better illustrate the behavior of the model, since the values of σ_{cre} and δ_f vary depending on the direction of the displacement in the new model. Example of a normalized stress-displacement figures produced by displacement sequence 1 are presented in Figure 47 a for the new model and b for the old model. The unloading happened in a straight line like it should happen, as presented in Figure 27. The softening continued when the stress reaches

the same ratio of $\sigma_{eff}/\sigma_{cre}$ as it had in the beginning of unloading. Similarly, the ratio u_e/δ_f was identical at the beginning of unloading and when the softening started again. This behavior was also expected with the old model, since the values of σ_{cr} and δ_f do not depend on the loading direction.

The stress-displacement (σ_{eff} - u_e) graphs for the new and old model are plotted in Figure 48 a and b respectively. These figures show how the models worked under the changing load direction. The graph a is not continuous like the normalized one. The σ_{eff} at which unloading started was different than the value of σ_{eff} at the end of reloading. Similarly the values of u_e

Table 11. The directions of the displacement sequences used in the unload-reload test

Test	1. Direction [°]	2. Direction [°]
1	6	60
2	65	35
3	25	130
4	50	-20
5	170	-15

Table 12. The dissipated energies with different unload and reload sequences for the old and new model.

Test	New G_e [J]	New G_I+G_{II} [J]	Original G_e [J]	Original G_I+G_{II} [J]
1	15.0	15.0	15.0	23.8
2	15.0	15.0	15.0	15.9
3	15.0	15.0	15.0	26.1
4	15.0	15.0	15.0	17.8
5	15,0	15.0	15.0	39.8

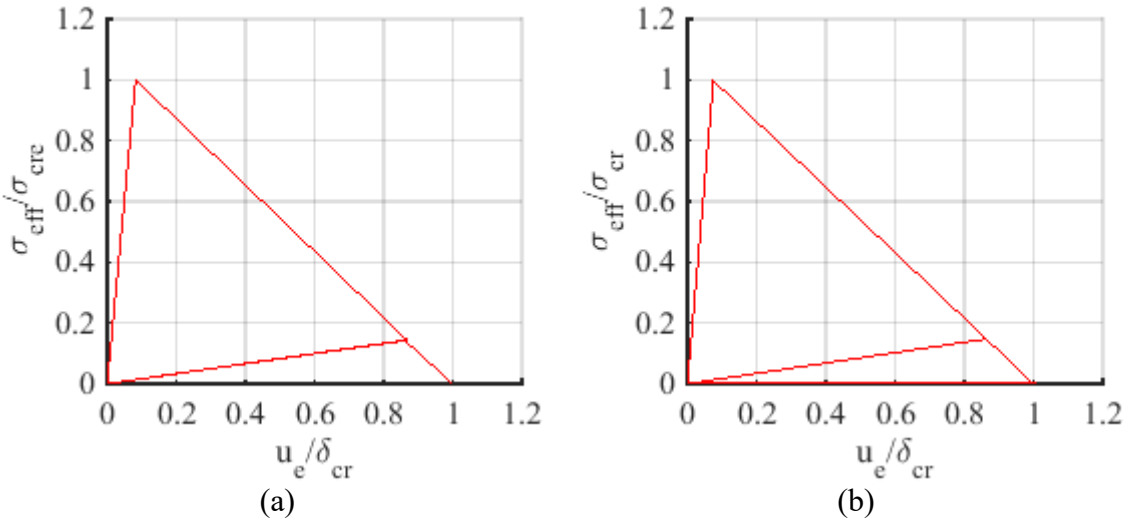

Figure 47. Example of normalized unload-reload behavior in case 1 with new model (a) and original model (b). The figures have otherwise similar shape, but the unloading starts with different stress ratio.

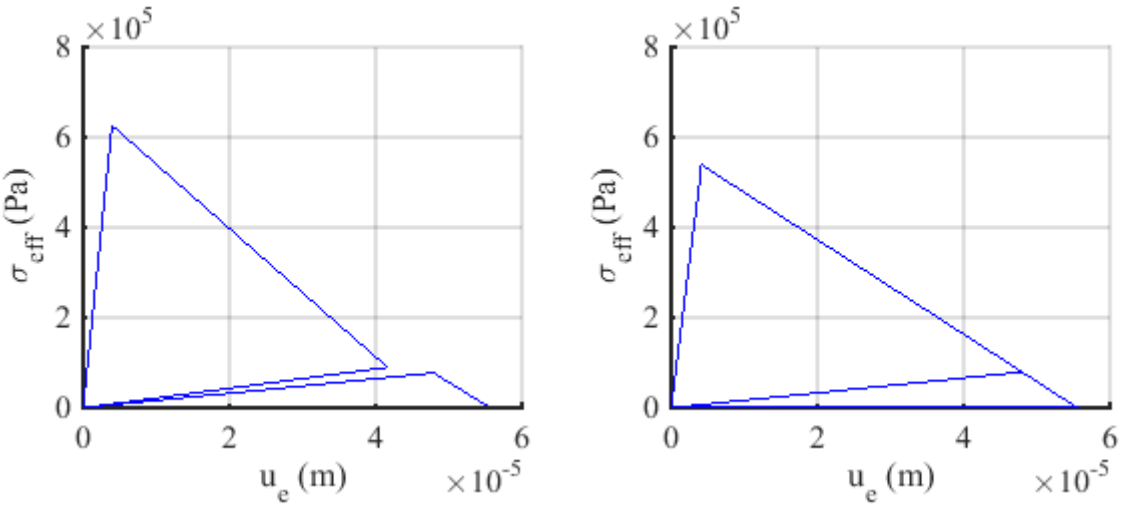

Figure 48. Example of the true unload-reload behavior in case 1 with new model (a) original model (b). The softening continues with different u_e in (a), which is not noticed in (b). The behavior is due to the changing δ_f.

were different at the start of unloading and end of reloading. This was due to the changing values of σ_{cre} and δ_f. The new model ensures that the softening continues when the values of δ and σ_{eff} reach the same ratio of the δ_f and σ_{cre} that were achieved when unloading began. The behavior of the original model in Figure 48 b was similar to the behavior presented in Figure 47 b. This was due to the values of δ_f and σ_{cr} not changing during the un- and reload process. The tests conducted show that the un- and reload behavior of the new model worked as intended.

5.5 Load direction change during softening process

The behavior of the model when load direction was changed during the softening was inspected by using a displacement sequence that changes its direction during the softening process. The sequences used work as follows: The model was first loaded monotonously in direction 1 for a fixed amount, after which the direction of the loading changes to direction 2. A total of five different sequences were used, and they are listed in Table 13, and sequence 1 is illustrated in Figure 49 as an example. Examples of the normalized σ_{eff}-u_e graphs for both the old and new models are plotted in Figure 51 a and b respectively. In these tests no unloading happened during the change of loading direction, which resulted in the normalized figures having similar shape to those presented in chapter 5.1. Both the old and new models

Table 13. The directions of the sequences that changing loading direction during the softening process.

Sequence	1. Direction [°]	2. Direction [°]
1	20	0
2	20	90
3	30	70
4	10	0
5	10	45

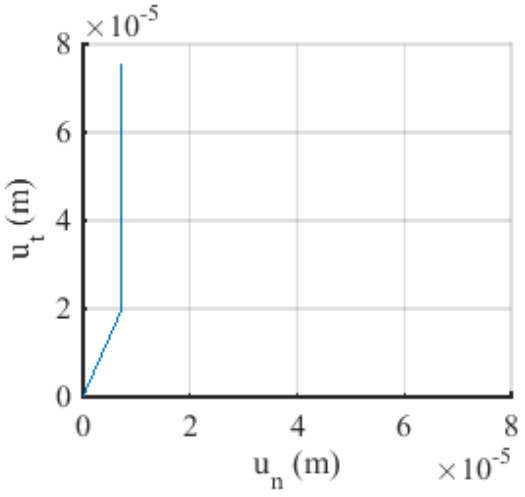

Figure 49. The shape of the vector used to test the load changing behavior.

have identical shapes. Examples of the σ_{eff} - u_e figures are presented in Figure 50 a and b. The graph a shows a slight bend in the softening part, which is marked with a black circle. Similar bends were observed with other displacement sequences. This was not observed with the original model. The amount of bending observed was higher when the load direction was in shear dominated.

The values for total dissipated energy for the new and original model are listed in Table 14. The dissipated energy values of the new model were not a constant 15 J, and they varied on both sides of the 15 J mark. The amount of error was not dependent on the used displacement step. The magnitude of the error was quite small, less than 3.7 % at highest, which was observed when the load direction was shear dominated. The magnitude of error decreased with decreasing amount of shear. Both dissipated energy forms gave almost equal results, with only small variation. These observations show that the new model does not work as it should when load direction changes during the softening process.

In the original model the effective dissipated energy was again correct. The components gave a much larger amount of energy dissipated. The dissipated energy values were much higher than the amount of error obtained from the new model. Similarly to the new model, the amount of error decreased with the decreasing amount of shear.

As was observed, the new model was found lacking when load direction changes during softening. The dissipated energy was less than what was expected, even though the element had opened fully. Although the magnitude of the error was quite small, the fact that it did not depend on the step size is important. Additionally, the magnitude of error was higher when the softening was dominated by shear. Since the softening started at the correct σ_{eff} and the final fracture also occurred with the right δ, this would hint that the return mapping does not work as it should when the load changes direction during the softening. Further research to this matter is therefore required.

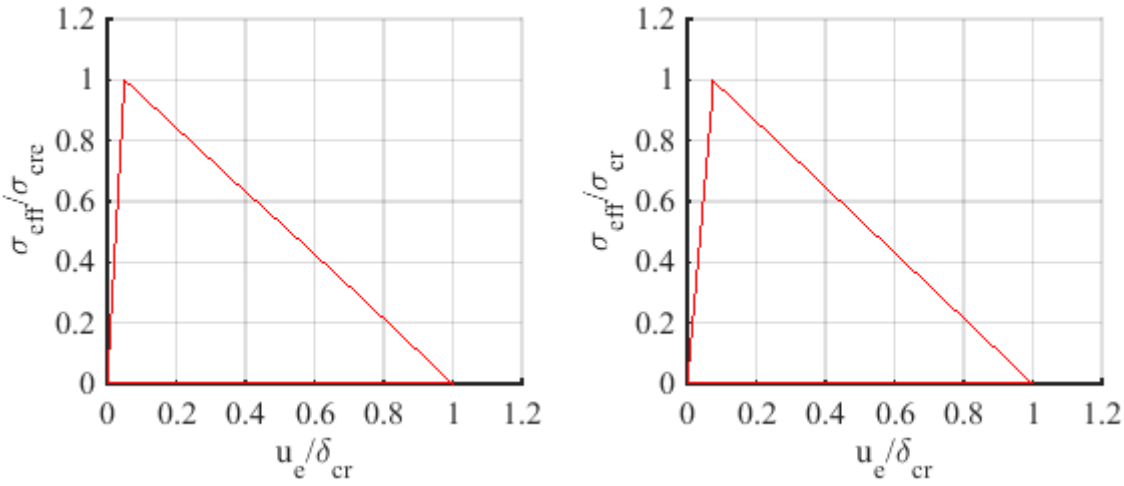

Figure 50. The behavior of the new (a) and original (b) models under changing load direction with true axes. A slight bend is observed in the softening part of (a), which is due to the change of loading direction. This is not observed in (b).

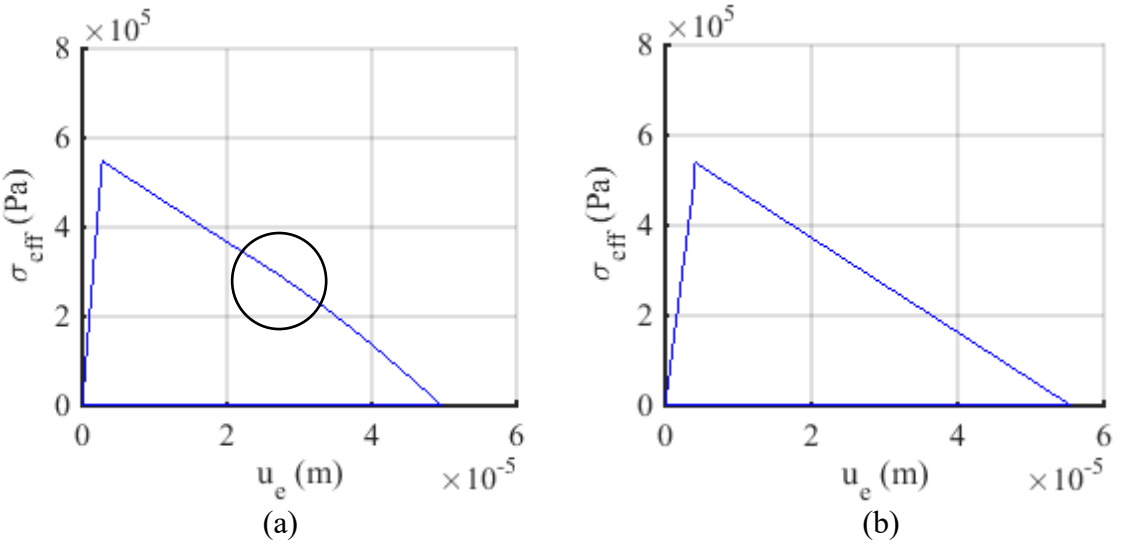

Figure 51. The behavior of new model (a) and original model (b) under changing load direction with normalized axes. The figures have identical shape. Black circle in (a) marks the location at which the load direction changes.

Table 14. The dissipated energies with changing load direction during the softening process. Both models gave incorrect dissipated energy values.

Sequence	New G_e [J]	New G_I+G_{II} [J]	Original G_e [J]	Original G_I+G_{II} [J]
1	14.5	14.4	15.0	44.8
2	15.1	15.1	15.0	28.1
3	15.0	15.0	15.0	23.6
4	14.7	14.7	15.0	53.1
5	15.6	15.6	15.0	39.3

5.6 Effect of displacement step size

The accuracy of energy dissipation depends on the step size as was noted in chapter 5.1, and the decrease is caused by the numerical stepping. The effect of step size on the accuracy of the new model can be demonstrated by calculating the mean error in energy dissipation using different material parameter combinations with different step sizes. This is plotted in Figure 52. As can be seen from the figure, the accuracy increased with decreasing step size. The step size used in most of the tests in this chapter was $6.67 \cdot 10^4$ mm, which falls to the right end of the figure. The magnitude of error in maximum σ and δ was observed to be almost equal, while the error in dissipated energy was much higher. The error decreased quite fast as the displacement step size decreased.

Since the energy is integrated from stress and displacement data, large displacement steps cause errors in the dissipated energy, which was observed with highly compressive case in Figure 46. The reason for this error is that the correct maximum stress is not reached due to the displacement step size, which defines the smallest change in the stress. The softening process starts before the maximum stress comes close to the critical stress value and the crack opens. The behavior of the model with large displacement step size was compared to

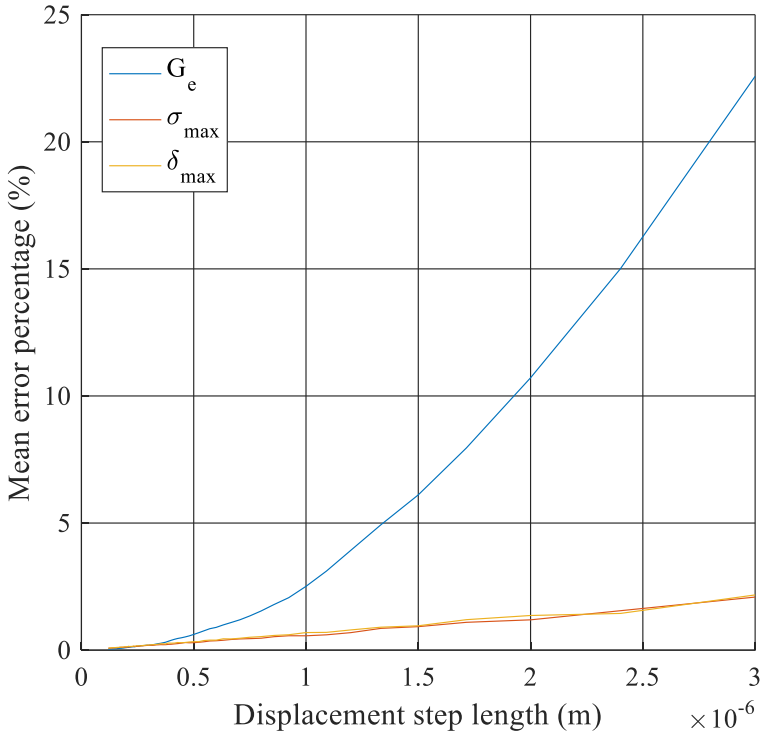

Figure 52. The dependence of accuracy in dissipated energy and maximum stress and COD on the used displacement length.

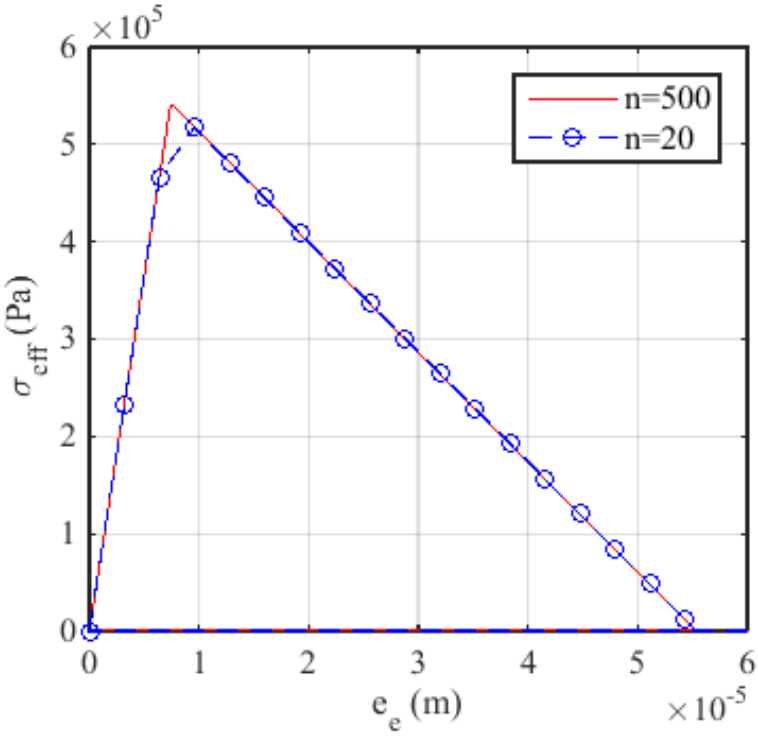

Figure 53. Stress-displacement graph of the new model with two different displacement step sizes.

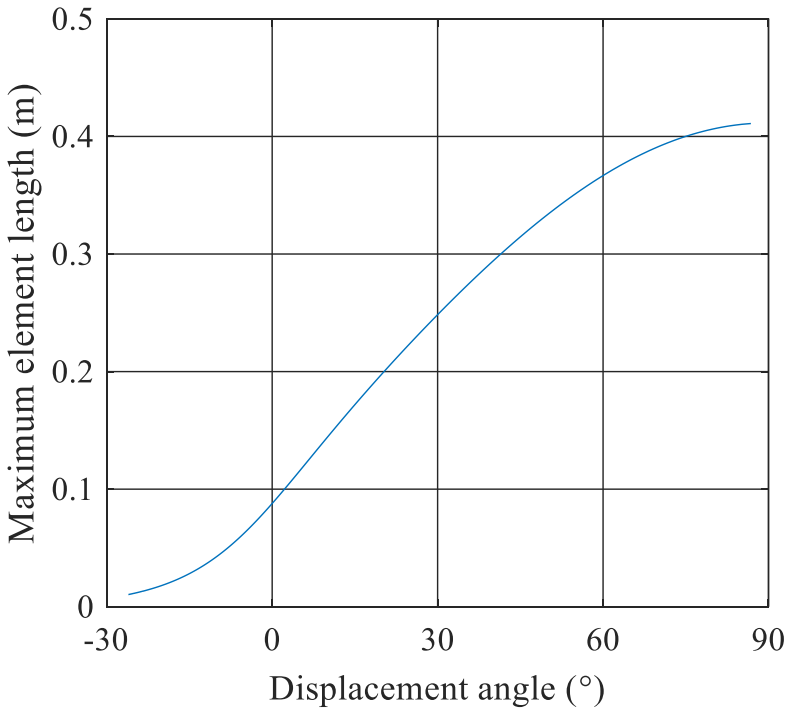

Figure 54. Maximum element length dependence on the displacement angle. The maximum element length decreases as the loading turns compressive at negative angels.

similar case with sufficiently small step size in Figure 53 to see whether the model works with too large displacement steps or not. As can be seen from the figure, with larger displacement steps the peak stress was missed, but the points still fell on the σ_{eff} - u_e graph created with sufficiently small steps. The figure shows that the model worked as intended even when the displacement step size is too large. However this means that the stress-displacement data cannot be used to calculate the amount of energy dissipated when the step size is too large.

5.7 Critical element length

The critical element length in the new model defined in Equation (33), and its value depends on σ_{cre}, which in turn depends on the angle α defined in Figure 26 a, as was noted in chapter 5.3. The angle α can be obtained from the angle β using the definition of stress components. The conclusion is that maximum L_0 depends on the loading direction β. To study the effect of loading direction on the maximum L_0, the value of maximum L_0 was plotted in Figure 54 with different loading directions using material parameters listed in Table 9. The figure shows that the value of maximum L_0 decreased from 0.4 m in tensile case to 0.08 m in shear case, which is only 20 % of the value in tensile case. The decrease continued as the amount of compression increased. At β = -30° the maximum element length was $1 \cdot 10^{-2}$ m. The decrease does not stop, since the magnitude of σ_{cre} increases as the amount of compression increases. Therefore the critical element length depends on the selected magnitude of allowed compression.

In the work of Paavilainen et al. (2011) an ice sheet with beam element length of 0.5 was used. With the selected element size range, the maximum allowable compressive stress would be 30 kPa when calculated with the material parameters used in this study. With larger compressive stresses the stability of the fracture model can become a problem. Therefore in possible future work either the compressive stress must be limited or the element size decreased.

5.8 Observations and analysis

The results presented show that the model created in this thesis works as intended, and improves on the behavior of the original model. The formulation of the new model works very much alike the original model, which should allow good easy implementation to the FEM-DEM code. The energy dissipated is correct regardless of the direction of the forced displacement. The dissipated energy can be calculated from either the effective stress and displacement, or the component values and summed. Both of these values need to be equal to the specific fracture energy given as material parameter. The new model satisfies this requirement, while the original does not.

It is important to note that both original and new model are approximate models that are intended to be used as part of a larger simulation, in which they performs very well. In the new model the δ_f depends on the load direction, which in turn leads to the actual length of current δ depending on load direction, as was described in chapter 4.2. This means that when the load direction changes, the actual crack opening displacement may decrease while the stress state moves on the yield surface. This results from the model using the ratio δ/δ_f to transmit the amount of δ reached between steps. The ratio stays constant when moving on a yield surface. This is non-physical behavior, but since the FEM-DEM code does not model the actual crack geometry in detail, the approximation used is acceptable.

When implementing the model into the FEM-DEM code, the time-step size should be sufficiently small that no significant errors will cumulate. The length of the time step should be small enough that the displacements that happen during the simulation are comparable to displacement steps used in the analysis. The new model works well even with quite large displacement steps, but this reduces the accuracy of energy dissipation. Therefore, if the amount of dissipated energy is studied, the step size must be sufficiently small.

When determining the element length for full analysis on the FEM-DEM code, the most important factor is how much compression the element can withstand. Increased compression decreases the maximum element length as was presented in Figure 54. A limit on the allowed compression should be enforced since this allows longer beam elements to be used in the analysis, which in turn allow smaller number of discrete elements to be used in the simulation. The discrete element number should be governed by other simulation parameters, and not the critical beam element length. Smaller number of discrete elements leads to faster calculation times.

6 Conclusions

As a result of this thesis an improved extrinsic cohesive crack model was created for the simulation of ice-structure interaction. The used cohesive crack model is based on the earlier work of Paavilainen et al (2009), with only minor changes to the basic definitions that lead to the final model. The aim was to improve the behavior of the original model in shear dominated cases, with main focus in the correct amount of dissipated energy due to the softening. The model was implemented to MATLAB, and its behavior was compared to the MATLAB implementation of the original model. The comparison was done using a forced displacement test on both the old and new models, and then comparing the results obtained. The models were compared in amount of dissipated energy as well as using the stress-displacement graphs.

The new model was observed to operate as intended, and was found to be better when compared to the original model. The only exception where the new model did not work correctly was the behavior when the load direction changes during the softening process. The original model was also found lacking with the changing loading direction. The new model was found to be more accurate when compared to the original model in these loading cases. The magnitude of error obtained with both models was observed to be higher when the direction of loading was shear dominated. The formulation of the new model lead to additional problem, which is the varying element length that depends on the load direction. The reason for this behavior is the use of effective critical stress that also depends on the loading direction. The problem does not exist in the original model. Overall the new model improved the operation in shear dominated loading cases, while working equally well in tensile cases.

When performing analyses with the newly created model, one must consider the amount of compression allowed in the model. As stated in chapter 5, the maximum beam element length depends on the loading direction and therefore the amount of allowed compression. Too big element lengths lead to numerical instabilities in the model. The restriction of compression is therefore important to avoid unnecessarily small element size which leads to long calculation times. The level of allowable compression can be selected based on the used beam element length.

Both the new and the original model were found to provide minor inaccuracies, which result from the used numerical scheme. The accuracy can be improved by decreasing the displacement step length. Additionally, the new model was found to follow the stress-displacement curve even with larger displacement steps. This is a positive feature, since it gives some room for error in larger ice-structure simulations, where the displacement steps become too large for a short time. This decreases the accuracy of maximum stresses, which could lead to additional problems with the DEM-stage, which calculates the forces applied to the elements based on the stresses in the beam elements.

Future work includes the implementation of the new model to the Aalto 2D FEM-DEM program. The model can then be validated further to ensure that it works as intended. As stated, the model does not work in as intended when the load direction changes during the softening process. This along with the decreasing critical element length in compressive cases are the only drawbacks found during the testing of the new model. The error with changing load direction is larger in shear dominated cases, and the magnitude of error is

somewhat acceptable. Most likely the error is caused by the return mapping algorithm, since the softening started with correct stress and ended with correct crack opening displacement in all of the test cases.

References

Abaqus., 2014. *Abaqus 6.14 Analysis User's Manual.* Providence, Rhode Island, USA: .

Alfano, G. and Crisfield, M.A., 2001. Finite element interface models for the delamination analysis of laminated composites: mechanical and computational issues. *International Journal for Numerical Methods in Engineering*, vol. 50, no. 7, pp. 1701-1736 ISSN 0029-5981. DOI 10.1002/nme.93.

Bathe, K., 1996. *Finite element procedures.* Prentice Hall International Upper Saddle River, NJ: 1037 p. ISBN 013349697X.

Bažant, Z.P. and Planas, J., 1998. *Fracture and size effect in concrete and other quasibrittle materials.* CRC Press Boca Raton [u.a.]: 616 p. ISBN 9780849382840.

Block, G., Rubin, M., Morris, J. and Berryman, J., 2007. Simulations of dynamic crack propagation in brittle materials using nodal cohesive forces and continuum damage mechanics in the distinct element code LDEC. *International Journal of Fracture*, vol. 144, no. 3, pp. 131-147 ISSN 0376-9429. DOI 10.1007/s10704-007-9085-2.

Borst, R.d. and Crisfield, M.A., 2012. *Nonlinear finite element analysis of solids and structures.* Wiley Chichester, West Sussex, United Kingdom: verkkoaineisto (1 online resource.) p. ISBN 9781118376010.

Camacho, G.T. and Ortiz, M., 1996. Computational modelling of impact damage in brittle materials. *International Journal of Solids and Structures*, vol. 33, no. 20, pp. 2899-2938 ISSN 0020-7683. DOI 10.1016/0020-7683(95)00255-3.

Camanho, P.P., Davila, C.G. and De Moura, M.F., 2003. Numerical Simulation of Mixed-Mode Progressive Delamination in Composite Materials. *Journal of Composite Materials*, vol. 37, no. 16, pp. 1415-1438 ISSN 0021-9983. DOI 10.1177/0021998303034505.

Carlsson, K., 2013. *Modeling of three dimensional microstructures including grain boundary mechanisms.* Chalmers University of Technology, Göteborg.

Carpinteri, A., Cornetti, P., Barpi, F. and Valente, S., 2003. Cohesive crack model description of ductile to brittle size-scale transition: dimensional analysis vs. renormalization group theory. *Engineering Fracture Mechanics*, vol. 70, no. 14, pp. 1809-1839 ISSN 0013-7944. DOI //dx.doi.org/10.1016/S0013-7944(03)00126-7.

Daudeville, L., Allix, O. and Ladevèze, P., 1995. Delamination analysis by damage mechanics: Some applications. *Composites Engineering*, vol. 5, no. 1, pp. 17-24 ISSN 0961-9526. DOI 10.1016/0961-9526(95)93976-3.

Dempsey, J.P. and Mulmule, S.V., 1997. Stress-Separation Curves for Saline Ice Using Fictitious Crack Model. *Journal of Engineering Mechanics*, vol. 123, no. 8, pp. 870-877 ISSN 0733-9399. DOI 8(870).

Espinosa, H.D. and Zavattieri, P.D., 2003. A grain level model for the study of failure initiation and evolution in polycrystalline brittle materials. Part I: Theory and numerical implementation. *Mechanics of Materials*, vol. 35, no. 3, pp. 333-364 ISSN 0167-6636. DOI 10.1016/S0167-6636(02)00285-5.

Falk, M.L., Needleman, A. and Rice, J.R., 2001. A Critical Evaluation of Cohesive Zone Models of Dynamic Fracture. *Jounal De Physique IV*.

Gálvez, J.C., Červenka, J., Cendón, D.A. and Saouma, V., 2002. A discrete crack approach to normal/shear cracking of concrete. *Cement and Concrete Research*, vol. 32, no. 10, pp. 1567-1585 ISSN 0008-8846. DOI 10.1016/S0008-8846(02)00825-6.

Guo, L., Xiang, J., Latham, J. and Izzuddin, B., 2016. A numerical investigation of mesh sensitivity for a new three-dimensional fracture model within the combined finite-discrete element method. *Engineering Fracture Mechanics*, vol. 151, pp. 70-91 ISSN 0013-7944. DOI 10.1016/j.engfracmech.2015.11.006.

Heinonen, J., 2004. *Constitutive modeling of ice rubble in first-year ridge keel.* VTT Technical Research Centre of Finland; VTT 142 p.

Hilding, D., J. Forsberg and A. Gürtner., 2011. Simulation of Ice Action Loads on Offshore Structures*8th European LS-DYNA Users Conference, Strasbourg, France*1-12.

Hillerborg, A., Modéer, M. and Petersson, P.-., 1976. Analysis of crack formation and crack growth in concrete by means of fracture mechanics and finite elements. *Cement and Concrete Research*, vol. 6, no. 6, pp. 773-781 ISSN 0008-8846. DOI 10.1016/0008-8846(76)90007-7.

Högberg, J., 2006. Mixed mode cohesive law. *International Journal of Fracture*, vol. 141, no. 3, pp. 549-559 ISSN 0376-9429. DOI 10.1007/s10704-006-9014-9.

Janssen, M., Zuidema, J. and Wanhill, R.J.H., 2004. *Fracture mechanics.* Spon Press New York: ISBN 9786610052851.

Kinnunen, A., Tikanmäki, M., Heinonen, J., Kurkela, J., Koskinen, P. and Jussila, M., 2012. Azimuthing thruster ice load calculation.

Klein, P.A., Foulk, J.W., Chen, E.P., Wimmer, S.A. and Gao, H.J., 2001. Physics-based modeling of brittle fracture: cohesive formulations and the application of meshfree methods. *Theoretical and Applied Fracture Mechanics*, vol. 37, no. 1, pp. 99-166 ISSN 0167-8442. DOI 10.1016/S0167-8442(01)00091-X.

Kolari, K., 2007. *Damage mechanics model for brittle failure of transversely isotropic solids. Finite element implementation.* VTT 195 p.

Kuutti, J. and Kolari, K., 2012. A local remeshing procedure to simulate crack propagation in quasi-brittle materials. *Engineering Computations Vol.29 Nr.2, 125 - 143* DOI 10.1108/02644401211206025.

Kuutti, J., Kolari, K. and Marjavaara, P., 2013. Simulation of ice crushing experiments with cohesive surface methodology. *Cold Regions Science and Technology*, vol. 92, pp. 17 ISSN 0165-232X. DOI 10.1016/j.coldregions.2013.03.008.

Lu, W., Lubbad, R. and Lose, S., 2014. Simulating ice-sloping structure interactions with the cohesive element method. *Journal of Offshore Mechanics and Arctic Engineering*, vol. 136, no. 3, pp. 31501 ISSN 0892-7219. DOI 10.1115/1.4026959.

Mulmule, S.V. and Dempsey, J.P., 1999. Scale effects on sea ice fracture. *Mechanics of Cohesive-Frictional Materials*, vol. 4, no. 6, pp. 505-524 ISSN 1099-1484. DOI AID-CFM67>3.0.CO;2-P.

Mulmule, S.V. and Dempsey, J.P., 1997. A Viscoelastic Fictitious Crack Model for the Fracture of Sea Ice. *Mechanics of Time-Dependent Materials*, vol. 1, no. 4, pp. 331-356 ISSN 1385-2000. DOI 1008063516422.

Nguyen, V.P., 2014a. Discontinuous Galerkin/extrinsic cohesive zone modeling: Implementation caveats and applications in computational fracture mechanics. *Engineering Fracture Mechanics*, vol. 128, pp. 37-68 ISSN 0013-7944. DOI //dx.doi.org/10.1016/j.engfracmech.2014.07.003.

Nguyen, V.P., 2014b. An open source program to generate zero-thickness cohesive interface elements. *Advances in Engineering Software*, vol. 74, pp. 27-39.

Paavilainen, J., Tuhkuri, J. and Polojärvi, A., 2011. 2D numerical simulations of ice rubble formation process against an inclined structure. *Cold Regions Science and Technology*, vol. 68, no. 1–2, pp. 20-34 ISSN 0165-232X. DOI //dx.doi.org/10.1016/j.coldregions.2011.05.003.

Paavilainen, J., Tuhkuri, J. and Polojärvi, A., 2009. 2D combined finite-discrete element method to model multi-fracture of beam structures. *Engineering Computations*, vol. 26, no. 6, pp. 578-598 ISSN 0264-4401. DOI 10.1108/02644400910975397.

Papoulia, K.D., Sam, C. and Vavasis, S.A., 2003. Time continuity in cohesive finite element modeling. *International Journal for Numerical Methods in Engineering*, vol. 58, no. 5, pp. 679-701 ISSN 0029-5981. DOI 10.1002/nme.778.

Park, K. and Paulino, G.H., 2012. Computational Implementation of the PPR Potential-based Cohesive Model in ABAQUS: Educational Perspective. *Engineering Fracture Mechanics*, vol. 93, pp. 239 ISSN 0013-7944. DOI 10.1016/j.engfracmech.2012.02.007.

Park, K., Paulino, G.H., Celes, W. and Espinha, R., 2012. Adaptive mesh refinement and coarsening for cohesive zone modeling of dynamic fracture. *International Journal for Numerical Methods in Engineering*, vol. 92, no. 1, pp. 1-35 ISSN 0029-5981. DOI 10.1002/nme.3163.

Park, K., Paulino, G.H. and Roesler, J.R., 2009. A unified potential-based cohesive model of mixed-mode fracture. *Journal of the Mechanics and Physics of Solids*, vol. 57, no. 6, pp. 891-908 ISSN 0022-5096. DOI 10.1016/j.jmps.2008.10.003.

Planas, J., Elices, M. and Guinea, G.V., 2004. 4 THE EXTENDED COHESIVE CRACK. *Fracture of Brittle Disordered Materials: Concrete, Rock and Ceramics*, pp. 51.

Reddy, J.N., 2014. *An Introduction to Nonlinear Finite Element Analysis.* Oxford University Press New York: 476 p. ISBN 0-19-852529-X.

Sam, C., Papoulia, K.D. and Vavasis, S.A., 2005. Obtaining initially rigid cohesive finite element models that are temporally convergent. *Engineering Fracture Mechanics*, vol. 72, no. 14, pp. 2247-2267 ISSN 0013-7944. DOI //dx.doi.org/10.1016/j.engfracmech.2004.12.008.

Schreyer, H.L., Sulsky, D.L., Munday, L.B., Coon, M.D. and Kwok, R., 2006. Elastic-decohesive constitutive model for sea ice. *Journal of Geophysical Research - Oceans*, vol. 111, no. C11, pp. C11S26 ISSN 0148-0227. DOI 10.1029/2005JC003334.

Schulson, E.M., 2001. Brittle failure of ice. *Engineering Fracture Mechanics*, vol. 68, no. 17, pp. 1839-1887 ISSN 0013-7944. DOI 10.1016/S0013-7944(01)00037-6.

Serré, N., 2011. Numerical modelling of ice ridge keel action on subsea structures. *Cold Regions Science and Technology*, vol. 67, no. 3, pp. 107-119 ISSN 0165-232X. DOI //dx.doi.org/10.1016/j.coldregions.2011.02.011.

Simo, J.C. and Hughes, T.J., 1998. *Computational inelasticity.* Springer New York: 392 p. ISBN 9780387975207.

Spring, D.W., 2015. *Failure processes in soft and quasi-brittle materials with nonhomogeneous microstructures.* University of Illinois at Urbana-Champaign 207 p.

Timco, G.W. and Weeks, W.F., 2009. A review of the engineering properties of sea ice. *Cold Regions Science and Technology*, vol. 60, no. 2, pp. 107-129 ISSN 0165-232X. DOI 10.1016/j.coldregions.2009.10.003.

Turon, A., Dávila, C.G., Camanho, P.P. and Costa, J., 2007. An engineering solution for mesh size effects in the simulation of delamination using cohesive zone models. *Engineering Fracture Mechanics*, vol. 74, no. 10, pp. 1665-1682 ISSN 0013-7944. DOI 10.1016/j.engfracmech.2006.08.025.

Tvergaard, V. and Hutchinson, J.W., 1992. The relation between crack growth resistance and fracture process parameters in elastic-plastic solids. *Journal of the Mechanics and Physics of Solids*, vol. 40, no. 6, pp. 1377-1397 ISSN 0022-5096. DOI 10.1016/0022-5096(92)90020-3.

van den Bosch, M J, Schreurs, P.J.G. and Geers, M.G.D., 2006. An improved description of the exponential Xu and Needleman cohesive zone law for mixed-mode decohesion. *Engineering Fracture Mechanics*, vol. 73, no. 9, pp. 1220-1234 ISSN 0013-7944. DOI //dx.doi.org/10.1016/j.engfracmech.2005.12.006.

Xie, D. and Waas, A.M., 2006. Discrete cohesive zone model for mixed-mode fracture using finite element analysis. *Engineering Fracture Mechanics*, vol. 73, no. 13, pp. 1783-1796 ISSN 0013-7944. DOI 10.1016/j.engfracmech.2006.03.006.

Xu, X.-. and Needleman, A., 1994. Numerical simulations of fast crack growth in brittle solids. *Journal of the Mechanics and Physics of Solids*, vol. 42, no. 9, pp. 1397-1434 ISSN 0022-5096. DOI 10.1016/0022-5096(94)90003-5.

Zhang, Z.(., Paulino, G.H. and Celes, W., 2007. Extrinsic cohesive modelling of dynamic fracture and microbranching instability in brittle materials. *International Journal for Numerical Methods in Engineering*, vol. 72, no. 8, pp. 893-923 ISSN 1097-0207. DOI 10.1002/nme.2030.

Zhou, F. and Molinari, J., 2004. Dynamic crack propagation with cohesive elements: a methodology to address mesh dependency. *International Journal for Numerical Methods in Engineering*, vol. 59, no. 1, pp. 1-24.

Appendix 1 Extrinsic crack algorithm MATLAB file

```
% sef = effective stress
% eff = effective strain
% f   = failure criterion
% dmc = maximum cod (current)
% dec = cod (current)
% stc = element status (current)
    %(1=undamaged, 2=some damage, 3=fully damaged)
% sig = stress matrix
% et  = tangential strain
% en  = normal strain

function [sef,epse,f,dmc,dec,stc,sig,et,en] =
extrinsic_crack_algorithm(dt,dn,dmz,L0,E,GS,G,sc,tc,st)
en   = dn/L0;       % normal strain
et   = dt/L0;       % tangential strain

sig(1) = GS*et;     % Shear stress
sig(2) = E*en;      % Normal stress

EE=E;               % Save Young's modulus
sc2=sc;             % Save the critical normal stress

epse =sqrt(en*en+et*et); % Effective strain
e1=et/epse;              % Tangential fraction of the total strain
e2=en/epse;              % Normal fraction of the total strain

E=sqrt(EE^2*e2^2+GS^2*e1^2);    %Effective Young's modulus

alp=atan(en*EE/(GS*et));        %Stress angle alpha

%Effective critical stress
    %The condition is for pure tension cases where sce goes to infinity
if(round(alp,10)==round(pi/2,10))
   sc=sc2;
else
   sc=(-(sin(alp)/sc2)+sqrt((sin(alp)/sc2)^2-4*(cos(alp))^2/tc^2*(-
1)))/(2*(cos(alp))^2/tc^2);
end;

df=2*G/sc;           % Critical crack opening
dtr = dmz*df;        % trial crack opening

str    = E*(epse - dtr/L0);   % trial stress
ftr    = str - sc*(1-dmz);    % trial failure criterion

if(ftr <= 0 && st == 1)        % elastic regime:  F<0 & status=intact
    dmc = 0;
    dec = 0;
    sef = str;              %Effective stress
```

```
    stc = 1;                %status update
```

```
elseif(ftr > 0 && dmz < 1)% cohesive softening: F>0 & status!=intact
    %new value for current crack opening displacement
    a   = E*epse/sc;
    b   = E/(sc*L0);
    dec = (a-1)/(b-1/df);

    sef = sc*(1-dec/df);  % new effective stress
    dmc = dec/df;         % new maximum cod ratio
    stc = 2;              % status update
    dec=dec/df;           % New current COD ratio

elseif(ftr <= 0 && st == 2) % unloading/reloading: F<0 & status!=intact
    % new value for current crack opening displacement
    a    = sc/E*(1/(dmz*df)-1/df);
    b    = 1/L0;
    dec  = epse/(a+b);

    sef = sc*(1-(dmz*df)/df)*dec/(df*dmz);   % new effective stress
    dmc = dmz;              % new maximum COD ratio
    stc = 2;                % status update
    dec=dec/df;             % New current COD ratio

else                        % Fully damaged
    dmc = 1;
    dec = 1;
    sef = 0;
    stc = 3;
    sig(1)     = 0;
    sig(2)     = 0;
end;

%Update stress components
    if(abs(sig(1)) < 1e-5)      % case of pure tension
        sig(1)  = 0;
        sig(2)  = sef;
    elseif(abs(sig(2)) < 1e-5)  % case of pure shear
        sig(1) = sef*sign(sig(1));
        sig(2)  = 0;
    else                        % mixed mode

        sig(2) = sef*(sin(alp));            %Normal stress component
        sig(1) = sef*cos(alp)*sign(sig(1)); %Shear stress component
    end;

f    = sef - sc*(1-dec);    %Failure criterion
end
```

Appendix 2 Test script MATLAB file

```
%Test script for a forced-displacement test
close all;      %Close all previous graphs and clear memory
clear all;

sc = 540e3;      % critival normal stress (sigma)
tc = 725e3;      % critical shear stress (tau)
G  = 15;         % fracture energy
L0 = 30e-3;      % Element length
E  = 4e9;        % Young's modulus
nu = 0.3;        % Poisson's coefficient
GS = 3*1e9;      % Shear modulus
n1  = 500;       % number of steps (in for loop below)
GS=E/(2*(1+nu)); % Calculate the shear modulus

beta=13*pi/180;  % Displacement angle beta

dfn=2*G/sc;                 %Max critical opening in normal mode
dft=2*G/tc;                 %Max critical opening in shear mode

if (L0>E*dfn/sc|| L0>GS*dft/tc)  %Error if element size is too large
    error1
end;

lend = max(2*G/sc,2*G/tc);  %Max forced displacement
len  = 0:1.2*lend/n1:1.2*lend;   %Define the displacement vector
n = length(len);       %Set the number of steps to correct value
len(1)=1e-24;          %Errors occur if len(1)=0, therefore set it to 1e-24

%Here, the forced displacement vectors are initiated
d(:,1) = cos(beta)*len';
d(:,2) = sin(beta)*len';

%Predefine the vectors used for faster operation
sig_eff  = zeros(n,1);
eps_eff  = zeros(n,1);
sig      = zeros(n,2);
st       = zeros(n,1)+1;
dm       = zeros(n,1);
dc       = zeros(n,1);
et       = zeros(n,1);
en       = zeros(n,1);
F        = zeros(n,1);

delta_t=zeros(n,1);
delta_n=zeros(n,1);
delta_e=zeros(n,1);

dtshear=zeros(n,1);
dtnorm=zeros(n,1);
```

```
dteff=zeros(n,1);
```

```
for i=1:n           %Iteration loop
    %Call the cohesive crack function

[sig_eff(i),eps_eff(i),F(i:end),dm(i:end),dc(i),st(i:end),sig(i,:),et(i),en(i)
] = extrinsic_crack_algorithm(d(i,1),d(i,2),dm(i),L0,E,GS,G,sc,tc,st(i));

    alp=atan(en(i)*E/(GS*et(i)));    %Stress angle alpha

    %Calculate the effective critical stress
    %Condition for pure tension cases where sce goes to infinity
    if (round(alp,10)==round(pi/2,10));
        sce=sc;
    else
        sce=(-(sin(alp)/sc)+sqrt((sin(alp)/sc)^2-4*(cos(alp))^2/tc^2*(-
1)))/(2*(cos(alp))^2/tc^2);
    end;

    %Collecting all the important parameters
    df=2*G/sce;                %Critical opening of the step
    delta_t(i)=dc(i)*cos(alp)*df; %Shear opening (delta_t)
    delta_n(i)=dc(i)*sin(alp)*df;  %Normal opening (delta_n)
    delta_e(i) = dc(i)*df;            %Effective opening (delta_e)

    %Effective Young's modulus
    Effe=1./sqrt((sin(alp)/(E)).^2+(cos(alp)/(GS)).^2);

    %Total post-peak displacements
    dtshear(i)=(sig(i,1)/GS*L0+delta_t(i));  %Total tangential displacement
    dtnorm(i)=(sig(i,2)/E*L0+delta_n(i));     %Total normal displacement
    %Total effective displacement

dteff(i)=sig_eff(i)/(sqrt((E*en(i)/eps_eff(i))^2+(GS*et(i)/eps_eff(i))^2))*L0+
delta_e(i);

    %Ciritcal element length
    Lcr=2*G*Effe/sce^2;

    if(st(i)>2)     %if the element is fully damaged, end the loop
        break;
    end;
end;

%Calculate fracture energies
FEde = trapz(dm.*df,sig_eff);      % Fracture energy due to effective delta
FEdt = trapz(delta_t(:),sig(:,1)); % Fracture energy (due to deltat)
FEdn = trapz(delta_n(:),sig(:,2)); % Fracture energy (due to deltan)

% Fracture energy (due to tangential displacement)
FEt=trapz(dtshear(:),sig(:,1));
% Fracture energy (due to normal displacement)
FEn=trapz(dtnorm(:),sig(:,2));
% Fracture energy (due to effective displacement)
```

```
FEe=trapz(delta_e(:),sig_eff);
```

```
%Initialize the graphs
set(0,'defaulttextfontsize',16)
set(0,'defaultaxesfontsize',12)
set(0,'defaultaxesfontname','Times')
set(0,'defaulttextfontname','Times')
set(0,'DefaultLegendFontSize',12,'DefaultLegendFontSizeMode','manual');
set(0, 'DefaultFigurePosition', [1000,500,290,250]);

%Tangential stress-displacement graph
figure (1)
hold on; grid on;
plot(et*L0,sig(:,1))
xlabel('d_{t} (m)')
ylabel('\tau (Pa)')
axis([0,6e-5,0,6e+5])

%Normal stress-displacement graph
figure (2)
hold on; grid on;
plot(en*L0,sig(:,2))
xlabel('d_{n} (m)')
ylabel('\sigma (Pa)')
axis([0,6e-5,0,6e+5])

%Effective stress-displacement graph
figure (3)
hold on; grid on;
plot(eps_eff*L0,sig_eff)
xlabel('d_{e} (m)')
ylabel('\sigma_{e} (Pa)')
axis([0,6e-5,0,6e+5])

%Effective stress-COD graph
figure (4)
hold on; grid on;
plot(dc*df,sig_eff)
xlabel('\delta (m)')
ylabel('\sigma_{e} (Pa)')
axis([0,6e-5,0,7.4e+5])


return;
```